Pulsed plasma deposition of Fe-C-Cr-W coating on high-Cr-cast iron: Effect of layered morphology and heat treatment on the microstructure and hardness

Pulsed plasma deposition of Fe-C-Cr-W coating on high-Cr-cast iron: Effect of layered morphology and heat treatment on the microstructure and hardness

V.G. Efremenko[a,1], Yu.G. Chabak[a], A. Lekatou[b], A.E. Karantzalis[b], K. Shimizu[c], V.I. Fedun[a], A.Yu. Azarkhov[d], A.V. Efremenko[a]

[a]*Department of Physics, Pryazovskyi State Technical University, Universitetskaya Street 7, Mariupol, 87500, Ukraine*

[b]*Department of Materials Science and Engineering, University of Ioannina, Ioannina, GR-45110, Greece*

[c]*Muroran Institute of Technology, Mizumoto-cho 27-1, Muroran-city, Hokkaido, 050-858 Japan*

[d]*Department of Biomedical Engineering, Pryazovskyi State Technical University, Universitetskaya Street 7, Mariupol, 87500, Ukraine*

Abstract

Pulsed plasma treatment was applied for surface modification and laminated coating deposition on 14.5wt%-Cr cast iron. The scopes of the research were: (a) to obtain a microstructure gradient, (b) to study the relationship between cathode material and coating layer microstructure/hardness, and (c) to improve coating quality by applying post-deposition heat treatment. An electrothermal axial plasma accelerator with a gas-dynamic working regime was used as plasma source (4.0 kV, 10 kA). The layered structure was obtained by alternation of the cathode material (T1 - 18 wt% W high speed steel and 28 wt% Cr-cast iron). It was found that pulsed plasma treatment led to substrate sub-surface modification by the

[1] Corresponding author, e-mail: vgefremenko@rambler.ru, tel. +038-066-9488325

formation of an 11-18 μm thick remelted layer with very fine carbide particles that provided a smooth transition from the substrate into the coating (80-120 μm thick). The as-deposited coating of 500-655 $HV_{0.05}$ hardness consisted of "martensite/austenite" layers which alternated with heat-affected layers (layers the microstructure of which was affected by the subsequent plasma pulses). Post-deposition heat treatment (isothermal holding at 950 ºC for 2 h followed by oil quenching) resulted in precipitation of carbides M_7C_3, M_3C_2, M_3C (in Cr-rich layers) and M_6C, M_2C (in W-rich layers). These carbides were found to be Cr/W depleted in favor of Fe. The carbide precipitation led to a substantial increase in the coating hardness to 1240-1445 $HV_{0.05}$. The volume fraction of carbides in the coating notably increased relatively to the electrode materials.

Keywords: pulsed plasma deposition, layered coating, microhardness, carbide, post-deposition heat treatment, SEM/EDX

Introduction

Plasma-assisted treatments belong to the most promising technologies of surface engineering. They can perform synchronous surface modification, strengthening and protective coating deposition on a variety of metallic materials [1-3]. Among these methods, the pulsed plasma techniques (PPTs) stand out due to the expanded capabilities of surface property improving arising from additional beneficial factors, such as shock-wave-induced strengthening and radiation stimulated diffusion [4-7]. PPTs may employ various devices based on different working principles of plasma flux generation [6, 7]. One of them is the electrothermal axial plasma accelerator (EAPA) with gas-dynamic working regime [8, 9]. EAPA generates a pulsed high voltage discharge in air with subsequent formation of plasma flux. Upon contact with the plasma, substrate subsurface modification takes place. As reported by Samotugin et al [2], surface heating of tool steels with high velocity plasma is followed by surface quenching, which results in the formation of a modified layer of super-

hard martensite [2, 4]. Furthermore, EAPA cathode material may be transferred by the plasma flux (atoms, ions, microdroplets) and deposited as a coating on a modified surface. EAPA has successfully been adopted for [8-11]: a) excitation of elastic pulses in the fluid, b) surface modification of steels, c) metallic nanostructure formation and d) protective coating deposition.

The composition and structure of the deposited coating largely depend on the EAPA cathode and inner channel materials, which are subjected to evaporation and/or melting under the electric discharge [11]. The amount of substance to be transferred by plasma flux, as well as the coating thickness, are strongly affected by the physical properties of the cathode material (thermal capacity and conductivity, melting temperature, evaporation temperature, vapor pressure, etc.) [10]. When the cathode consists of a refractory material (graphite, W, Mo etc.), then evaporation is mostly responsible for the substance transfer [12]; as a result, thin and non-uniform coatings are formed. If the cathode material melting point is lower than that of a common refractory material, evaporation could be accompanied by cathode melting, which results in micro-droplet transportation via plasma flux; thus, thicker and more uniform coatings are formed. By combining different cathode materials in an alternating mode of deposition, it is possible to deposit multi-layered coatings with gradient microstructure and properties. The formation of gradient structures is reported as a most promising approach to improve the tribological behavior of many materials, such as ceramic composites [13, 14], alloys [15], coatings [16]. A post-deposition heat treatment can also be considered as a complementary stage for improving coating properties [17, 18]. Investigations focused on the selection of a proper EAPA cathode material for multi-component coatings with desired properties, as well as on the effect of post-deposition heat treatment are so far in initial stages.

High-chromium cast irons (HCCI) are well-known materials for tribotechnical applications. They are characterized by high wear resistance due to the presence, in their structure, of significant volume fractions (VF) of hard phases - carbides, nitrides, borides etc.

[19-21]. As a rule, these alloys are subjected to bulk heat treatment (HT) in order to increase their hardness and wear performance [22, 23]. However, the HT HCCIs do not always meet the growing demands for operational durability. The improvement of HCCI tribological properties could be based on surface engineering approaches, in particular, on the use of plasma-assisted technologies. Plasma treatment has been shown to be highly effective for surface hardening of a casting made of gray or ductile cast iron [24, 25]. Nevertheless, adopting plasma-assisted treatments for HCCI strengthening still remains essentially unstudied. Taking into account the above considerations, a multi-layer coating resulting from the combination/alternation of two cathode materials (T1 high speed steel and super-high Cr cast iron) was deposited on an HCCL by EAPA aiming to investigate: a) the relationship between cathode material and coating layer microstructure/hardness and b) the effect of post-deposition heat treatment on the coating features.

2. Materials and methods

HCCL was used as a substrate; its nominal composition is presented in Table 1. As cast HCCL in the form of plates of dimensions of 10x10x25 mm was subjected to annealing at 650 ^{o}C for a period of 20 h [26]. After heat treatment (HT), the specimens were polished (R_a=0.2 μm) to remove 0.5 mm of decarburized upper layer.

Coating deposition was carried out by EAPA-PPT. The EAPA principle scheme is given in Fig. 1a. EAPA is a paper reinforced bakelite tube (1) of 430 mm length, 8 mm inner diameter and 17 mm wall thickness. The tube is pressed by steel shells (3) and (4); shell (4) is used as an anode. Changeable rod (2) of 5 mm diameter, serving as a cathode, is positioned in the inner channel at a distance of 50-70 mm from the exit edge (5). In Fig. 1b, the electric installation of the EAPA assembly is shown; it is composed of an impulse voltage generator (IVG) (consisting of capacitive energy storage, a triggered spark gap, a pulse transformer, a decoupling capacitor) and an impulse current generator (ICG) (consisting of capacitive energy

storage and nonlinear inductance). The working voltage was 4.0 kV, the operating pressure was atmospheric and the working gas was air. A high-current (10 kA) pulsed arc discharge with a life duration of 0.8 ms [10] was generated between the cathode and the anode in the inner dielectric channel. The distance from the EAPA edge to the substrate was 50 mm. The time interval between pulses was 15 seconds to charge the capacitor.

Two alloys were used as cathode materials alternately deposited in the coating: T1 high speed steel (W18) and super-high Cr cast iron (Cr28). Their chemical compositions are given in Table 1. Regarding the W18 cathode, the tail portion of commercial T1 high speed steel (HSS) drill of 5 mm diameter was used in the as-manufactured state. Regarding the Cr28 cathode, a cast rod of 5 mm diameter was used in the as-cast state. The carbide volume fractions (CVF) of the cathode alloys are also included in Table 1.

The cathode materials were selected on the following grounds:

(a) The coatings to be formed should have a higher content of strong carbide-forming elements in relation to their substrate, so that, higher carbide volume fractions (chromium rich carbides (M_7C_3, $M_{23}C_6$) or tungsten rich carbides (M_6C, M_2C)) and, consequently, a higher wear resistance could be attained.

(b) The coatings to be formed should have an appreciable thickness due to the relatively low cathode melting point (in comparison with the melting point of a cathode consisting of a refractory material). As aforementioned in the Introduction, the lower the solidus temperature the easier cathode melting, thus enhancing micro-drop transfer and, consequently, coating thickness.

The solidus temperature of T1 steel was determined as the temperature of "L$\rightarrow$ austenite + M_6C" eutectic reaction [27], which had been estimated by Halfa [28] to take place at 1342 ^{o}C. This also follows from Fig. 2 which presents the equilibrium temperature-concentration phase diagrams of the systems Fe-18%W-4%Cr-1%V-C and Fe-28wt%Cr-2wt%Mn-1.3wt%Si-C, calculated using the Thermo-Calc software. As shown in Fig. 2b, eutectic reaction "L $\rightarrow$

(austenite + M_7C_3)" occurs at 1293 °C. Hence, solidus temperature values for W18 and Cr28 are found to be much lower as compared to that of the refractory materials (graphite (~3700 °C), W (3422 °C), Mo (2623 °C)), which usually serve as cathode in plasma-generating devices. Therefore, it is expected that employing W18 and Cr28 in the PPT process would result in enhanced microdroplet-mass transferring.

The final coating was obtained after eight impulses. In order to achieve a laminated gradient coating, the cathodes were alternately substituted after every two impulses as follows: 1st and 2d impulses were carried out with W18; 3d and 4th impulses – with Cr28; 5th and 6th impulses – with W18; 7th and 8th impulses – with Cr28 (2 pulses per coating layer). Coating deposition was followed by bulk HT: the specimens were heated up to 950 °C, retained at this temperature for 2 h and, then, oil quenched. HT was conducted in dry air while the specimens were covered by charcoal carburizing material in order to prevent surface oxidation**.** The PPT-treated specimens were investigated both in the as-deposited and HT states.

An optical microscope (OM) Nikon Eclipse M200 and scanning electron microscope (SEM) Ultra-55 (Zeiss) were employed for the coating microstructure examination. Cross-sections of coating samples were polished on the ATM GmbH preparation equipment according to a standard metallographic procedure and, then, they were etched by 4 vol.% nital. The carbide volume fraction (CVF) was calculated on the basis of SEM micrographs using Rosiwal's lineal analysis [29]; the procedure is analytically described in [30].

Phase chemical composition and chemical element distribution were investigated by energy dispersive X-ray spectrometry (EDS) using the JSM-6510 LV SEM (JEOL)/X-Act detector (Oxford Instruments) system, under a voltage of 20 kV and a working distance of 16 mm. Each phase chemical composition value is the average of four to five measurements obtained from different points and different fields of view.

Micro-hardness measurements were performed at the FM-300 (Future-Tech) tester, employing an external load of 0.05 kg. The microhardness profile (coating cross-actions) was

obtained by averaging the results of measurements along 7 lines perpendicular to the coating surface in different coating points.

Phase identification was carried out by X-Ray Diffraction (XRD) using the DRON-3 diffractometer (Bourevestnik Inc.) equipped with Fe-Kα radiation (λ=1.9373 Å) source. The diffraction angle step was 0.5 grad and the scanning velocity was 1 s per step. XRD-scanning was performed at a voltage of 20 kV and a filament current of 20 mA.

3. Results

3.1 Microstructure of the substrate and cathode materials

The initial microstructure (i.e. before plasma treatment) of the HCCL substrate was that of «pearlite+M_7C_3» eutectic and dendrites consisted of pearlite (Fig. 3a). The presence of the just mentioned structural components is in agreement with the result of earlier study [31] concerning HCCL of approximately the same chemical composition (2.7 wt% C; 14.55 wt % Cr; 2.2 wt % Mn, 0.93 wt % Ni) also annealed at 650 ^oC. The matrix microhardness was measured as 450±31 $HV_{0.05}$.

The microstructure of the W18 cathode consisted of bulky and fine carbides distributed in a metallic matrix (Fig. 3b). According to [32], the microconstituents of heat treated T1 HSS are martensite and M_6C (predominant amount), MC, $M_{23}C_6$ carbide phases. The CVF was measured as 16 vol. %. The microhardness of the W18 cathode material was measured as 945±25 $HV_{0.05}$.

The microstructure of the Cr28 cathode is shown in Fig. 3c. As can be seen, Cr28 is a hypoeutectic cast iron consisting of eutectic carbide and pre-eutectic dendrites of solid solution. XRD analysis revealed the presence of austenitic matrix, M_7C_3 and M_3C_2 carbides with the latter being of minor amount (Fig. 4, Table 2). The eutectic carbide VF was 34.5 vol.%. The matrix microhardness was measured as 335±21 $HV_{0.05}$.

3.2. Microstructure characterization and microhardness measurements

Fig. 5a shows the microstructure of the as-deposited coating (optical, cross-section). As can be seen, the PPT resulted in the emergence of a light contrast layer ("white layer") of 80-120 μm thickness on the top of substrate. The white layer has a laminated texture, composed of alternating bright contrast ("white") and relatively dark ("gray") bands. Gray color is due to more intensive etching in areas of very fine structure of dark contrast (Fig. 5b). A distinguished feature of this structure is a fine network of precipitates surrounding the grain boundaries (Fig. 5c). Occasionally, roundish shrinkages are revealed inside the coating (Fig. 5a). The free surface of the coating is wave-shaped. A clear boundary line between coating and substrate cannot be seen: the layer, which lies closest to the substrate, smoothly adjusts to the substrate structure.

Fig. 5d shows that the post-deposition HT resulted in a drastic alteration of the coating microstructure. Nital-etching revealed that the coating consists of five heterogeneous layers obviously differing from each other. The top layer, presenting the brightest contrast, is layer A; its thickness is 15-25 μm. Similar morphological features are observed in layer C, which is lying in a distance of 30-50 μm from the coating surface. These two layers are separated by layer B of 15-25 μm thickness with coarser structure / bulkier "white" phase. Below layer C, a relatively dark layer (of darker contrast than layers A, B and C), layer D, is observed consisting of quite large light microareas against a darker background; the thickness of layer D is 14-30 μm. Below layer D, the light contrast dispersion becomes fine, dense and uniform, defining a layer adjacent to the substrate, layer E; layer E has a homogeneous appearance and a thickness of 11-18 μm. The absence of clearly defined boundaries between all the layers should be highlighted.

The microhardness profile of the as-deposited coating is presented in Fig. 6 (the black solid lines correspond to the plots of the mean values). Fig. 6a shows that the measured microhardness values are widely dispersed within the range of 500-655 $HV_{0.05}$ with an average

value of 560 $HV_{0.05}$ through the bulk of the coating. The large scatter of microhardness values is mostly owing to the laminating structure of the coating: generally, the microhardness of the "white" bands is about 50 $HV_{0.05}$ higher than that of the "gray" bands. Along the narrow layer delimiting the coating and the substrate, microhardness increases up to 700-750 $HV_{0.05}$; after that, it drops to 420-480 $HV_{0.05}$ stabilizing at this level in the bulk of substrate.

Fig. 6b manifests significant strengthening of the coating caused by the HT-due microstructural changes. Layer A possesses microhardness of 1240-1360 $HV_{0.05}$ with a mean value of 1300 $HV_{0.05}$. The highest microhardness values were measured in layer B (1265-1445 $HV_{0.05}$ with a mean value of 1400 $HV_{0.05}$). Microhardness through layers C, D and E decreases monotonically with depth, reaching 950-1050 $HV_{0.02}$ in layer E. The substrate has a microhardness of 730-930 $HV_{0.05}$ with a mean value of 800 $HV_{0.05}$, which is much lower than that of the coating but almost double the hardness of the substrate before HT.

A more detailed characterization of the HT coating microstructure can be accomplished using SEM observation (Fig. 7). Figs. 7a and 7c reveal great amounts of light contrast precipitates in layers A and C, respectively. In layer A, the precipitates form a massive net engulfing dark matrix grains; small roundish precipitates are seen inside matrix grains too. Layers B and D contain bulky light-colored contrast precipitates (1-4 μm in cross-section), which are surrounded by the matrix areas (Fig. 7b, 7d). A distinguished feature of the microstructure of layer B and D is the presence of numerous very fine (0.03-0.5 μm in cross-section) precipitates of bright-white contrast uniformly distributed within the matrix; some of them (mostly larger ones) are situated along the contour of the bulky precipitates. The needles of martensite are also discerned in the matrix of layers B and D (Fig.7b).

The volume fraction of precipitates in the HT coating varies with the layer depth. As shown in Table 2, the highest precipitate VF is found in layer A – 61.3 vol.%; the precipitate VF in layer C is somewhat lower (55.4 vol.%), whilst the lowest precipitate VF is found in layer E (21.7 vol.%).

3.3. Chemical element distribution

EDS mapping of the coating cross-section (after HT) showed that the observed laminated structure has been caused by an uneven chemical element distribution. Fig. 8 illustrates the distribution of chromium, tungsten and iron within the coating. A comparison of these Figures with Fig. 5d reveals that the “layer-to-layer” transition is owing to the alteration of chromium and tungsten concentrations. Thus, layers A and C are enriched with chromium; they are separated by layer B which contains higher tungsten at the expense of chromium. Between layers C and D, a narrow diffusion zone is discerned with intermediate Cr and W contents. Layer D is enriched with tungsten, whilst impoverished in chromium. In contrast, adjoining (substrate and coating) layer E is poor in tungsten, while its chromium content is much lower comparing to layers A and C. Therefore, layer E can be identified as the transition zone between the coating and the substrate. Iron mapping shows that the concentration of Fe from the middle of the transition zone to the substrate surface is notably higher than that from the top of the coating to the middle of the transition zone. The gradient of the Fe concentration constitutes a strong evidence of the good coating/substrate adhesion.

The described distribution of Cr and W is the outcome of deposition with alternating cathode material; namely, layers A and C were deposited using Cr28 cathode, whereas layers B and D were obtained using W18 cathode. This is a major reason for the higher CVF contents in layers A and C as compared to layers B and D (Table 2). Cr28 cathode has higher content of carbon than W18 cathode (Table 1), allowing for higher CVFs in the resulting layers A and C.

Layer E origination was of special interest to be studied and discussed. The interlayer area between layers D and E is shown in Fig. 9 in higher magnification. As it can be seen from the secondary electron (SE) image (Fig. 9a), layer E includes net-shaped precipitates, which are similar to the precipitates of layers A and C. Additionally, massive eutectic carbide particles are observed within layer E. The distribution of elements with regard to their atomic number Z was evaluated by back scattered electron (BSE) imaging. According to Fig. 9b, carbide particles in

layer D are brighter than their matrix, thus they are bound to be enriched with heavier element (presumably, W with Z=74); the very bright contrast of the fine carbide particles indicates their higher content of tungsten. In contrast, layer E has a darker contrast throughout its volume, reflecting its relatively high content in lighter elements (Cr and/or Fe). (Indeed, Fig. 8 shows that layer E is richer in Cr than layer D.) Massive eutectic carbide particles and matrix appear dark, i.e. they are enriched with chromium (Z=24), while the net-shaped precipitates appear slightly brighter, i.e. they are enriched with iron (Z=26). So, layer E contains very few massive eutectic carbide particles; besides, it is poor in tungsten. Based on this observation, it is indicated that layer E is a modified substrate sub-surface layer, which was formed as a result of surface melting induced by the first plasma impulse using W18 cathode. Surface melting led to a eutectic carbide dissolution followed by smaller carbide precipitation during heat treatment. The above indication is in agreement with the low microhardness of layer E as compared to that of the other coating layers (approaching the microhardness of the substrate). To conclude, the presence of transition layer E (manifested by gradients in microstructural features (Table 2), microhardness (Fig. 6b) and chemical composition (Fig. 8) strongly suggest the high adhesion of the coating to the substrate. Moreover, the coating interlayer transition zones noted in Fig. 8 are considered to reduce interlayer stresses and increase interlayer adhesion as well.

3.4. XRD- and EDS-analysis

The XRD diffractograms of the coatings in the as-deposited and HT states are given in Fig. 10. The XRD-pattern of the as-deposited coating surface (Fig. 10a) shows that the top of coating consists of matrix phases γ-Fe (austenite) and α-Fe (ferrite) and carbide phases - M_3C, $M_{23}C_6$. Peak intensities indicate that γ-Fe and cementite are the main matrix and carbide phases, respectively. Austenite peak (111) is shifted to diffraction angles smaller those observed for the PDF cards. This behavior could be attributed to a supersaturated state of austenite as a result of its fast solidification upon deposition. Analogous XRD features were reported by

Totten et al. [33] regarding austenite supersaturated with nitrogen after plasma nitriding. It is most likely that α-Fe is martensite (i.e. distorted ferrite), as suggested by the diffraction angles, which are slightly displaced from the ones corresponding to α-Fe, according to the PDF cards and the increased microhardness of the as-deposited coating. The microhardness values achieved are 600-655 $HV_{0.05}$, which are almost three times higher than those of highly-alloyed austenite in non deformed Hadfield steel (215-230 HV) [34].

The XRD pattern of heat treated top layer A (deposited with Cr28 cathode) manifests that martensite has become the main matrix phase and M_7C_3 the main carbide phase. The carbide presence is more abundant in comparison with as-deposited layer A, as deduced from the higher intensities and occurrence of the respective peaks, most likely due to diffusion of C and Cr from the supersaturated austenitic lattice to the carbide phases during HT. Cr diffusion has led to the precipitation of carbides that can accommodate higher amounts of Cr in their structure (Cr_3C_2, $M_{23}C_6$ and M_7C_3) [35] than M_3C (predominating carbide stoichiometry in as deposited layer A). Therefore, the XRD patterns are compatible with the microhardness data (compare Figs. 6a and 6b). More analytically, the peaks of carbides M_7C_3, Cr_3C_2, $M_{23}C_6$ and M_3C are revealed (Fig. 10b). Some of these peaks may be assigned to more than one carbide types, making, thus, carbide identification difficult. Anyway, four strong peaks can uniquely be assigned to (320), (330), (202), (731) peaks of M_7C_3. Similarly, some peaks can uniquely be assigned to (301), (311) peaks of M_3C and (140), (002) peaks of Cr_3C_2. Based on the XRD results, it is indicated that the net-shaped carbides shown in Fig. 7a are mostly hexagonal Cr-rich M_7C_3 carbides. The predominance of M_7C_3 over $M_{23}C_6$ and Cr_3C_2 is attributed to the fact that the free energy of formation of chromium carbides follows the order: $\Delta G_f^o(Cr_7C_3) < \Delta G_f^o(Cr_{23}C_6) < \Delta G_f^o(Cr_3C_2)$ [36]. The metallic matrix in HT layer A consists of austenite and α-Fe (martensite); according to the relative intensities of α-Fe and γ-Fe reflections, martensite is the predominant phase in the matrix.

The diffractogram of coating layer D was received after smooth polishing to remove

layers A, B and C. Layer D, deposited with W18 cathode, contains carbides M_6C (Fe_3W_3C), M_2C (W_2C) and M_3C (Fig. 10c). The highest carbide peak intensity (511) corresponds to M_6C, whereas the lowest one (141) corresponds to M_3C. The metallic matrix is mostly martensitic. Minor peaks (002) and (003) are assigned to M_2C. Based on these results, it is strongly suggested that the bulky precipitates in Fig. 7d are M_6C-type, while the fine sized bright W-rich precipitates are M_2C-type.

XRD analysis was supplemented by EDS point analysis. Table 3 lists the extracted chemical compositions of matrix and carbides in the different coating layers. Here, it should be noted that the analyzed phases (especially the matrix) were dimensionally less than the spatial resolution of EDS quantitative analysis, as shown in Fig. 11. So, it is acknowledged that the quantitative EDS results do not exactly characterize the chemical composition of the phases because their composition is likely affected by the surrounding areas; however, they can reveal qualitative trends and rough differences. Furthermore, carbon analysis is not included in Table 3, because EDS quantitative analysis of carbon in an electron microscope is difficult, owing to the low energy of the Carbon x-ray K line and its consequent easy absorption, as well as hydrocarbon contamination [37].

As presented in Table 3, the phases of layer A are enriched with chromium: its concentrations in carbides and matrix have been measured as 30.2 wt% and 25.6 wt%, respectively. The latter value is probably excessive because of the effect of the carbide net that surrounds the small matrix areas (0.1-1 μm in diameter). It is noted that 3.0 wt% W was found in the carbides despite layer A–having been deposited with Cr28 cathode. Manganese is partitioned between matrix and carbides with a slight prevalence in the carbide phase. Approximately the same alloying element distribution was observed for layer C, as well.

The matrix of layer B was found slightly alloyed with tungsten (0.9 wt%) while the chromium content (13.9 wt%) was lower as compared to layer A. The carbides in layer B are alloyed with tungsten and chromium: bulky carbides contain 26.9 wt% Cr and 15.4 % W,

whereas fine carbides contain 12.4 % Cr and 40.3 wt % W. Thus, fine carbides are enriched with tungsten, which proves the BSE observation (Fig. 9b). The qualitative diferences of the W concentration in the matrix, bulky carbide particles and fine carbide particles are demonstrated in the EDS spectra of Fig. 12. Although layer B was deposited using W18 cathode, relatively high chromium contents in its phases are noted, supposedly due to Cr diffusion from adjacent layers A and C. Enrichment of bulky M_6C particles with chromium lowered iron content (as compared with layer D) which presumably provided the increased carbide hardness. This sequence of diffusion events can explain the maximum on microhardness profile assigned to layer B (Fig. 6b). More specifically, the highest hardness of layer B (despite the CVF that is lower than that of layers A and B) is mostly attributed to: a) the high contents of W and Cr in both bulky and fine carbide precipitates, and b) the fine dispersion of W-rich carbides in the matrix.

In comparison with layer B, the matrix in layer D presents higher tungsten and lower chromium concentration. The carbide particles in layer D were found to be enriched with iron and depleted of carbide-forming elements: the bulky carbides were found depleted of Cr by more than 50 %; the fine carbides were found depleted of W by nearly 10 wt%. The latter is assumed as underestimating: due to the small size of the fine carbide particles, EDS analysis results have (most likely) greatly been affected by the surrounding matrix. In general, layer D presents the lowest hardness amongst layers A, B and C mostly because of the lowest CVF.

Table 3 presents the chemical formulae for bulky carbide in the coating layers, as determined by XRD and EDX. The chemical formulae for fine carbides are not included in this table because of possible higher error in the elements content determination mentioned above.

4. Discussion

4.1. As-deposited coating

The data presented above show that pulse plasma treatment has led to a modified (by melting) sub-surface zone of HCCL. This modified zone has acted as an underlayer for the PPT coating providing a smoother transition from the substrate to the coating microstructure. Due to the high temperature of the plasma flux, each deposited layer melts down the previously deposited layer, thereby forming a multilayer coating, where interlayer boundaries are fused together, as follows from the microstructure observations.

According to evaluation by Kolyada et al. [11], the temperature of plasma in EAPA reaches 10000 K that is higher than the melting point of carbides (2730 ^{o}C – for W_2C and 1755 ^{o}C – for Cr_7C_3 [38]). Thus, the electric discharge inside EAPA could cause complete melting (dissolution) of carbides in a thin layer of the cathode surface subjected to plasma heating. This assumption has been proved by microscopic examination of the as-deposited coating, which showed the absence of any coarse carbide that pre-existed in the raw materials (compare Figs. 3b, c with Fig. 5a).

Melted-evaporated cathode substance was transferred to the substrate surface to be rapidly solidified. In equilibrium conditions, alloys W18 and Cr28 solidify according to eutectic reactions "L$\rightarrow$austenite+M_6C" (W18) and "L$\rightarrow$austenite+ M_7C_3" (Cr28) that result in eutectic carbide crystallization (Fig. 2). During PPT-deposition, this mechanism changed because of ultra-fast ion condensation and microdroplet crystallization on the substrate surface. In the condition of suppressing of atom movement, the appearance of eutectic carbides became kinetically unfavorable, thus carbon and carbide-forming elements were retained in liquid state until the end of solidification. This resulted in a coating with a structure consisting of supersaturated austenite and α-Fe-based solid solution (Fig. 10a).

A similar "solute trapping" effect has been observed by Fenech et al. [17], Hemmati et al. [39], Vamsi Krishna and Bandyopadhyay [40] in coatings deposited by different laser

deposition techniques. These authors have noted the necessity of post-deposition HT to decompose supersaturated matrix in order to improve coating properties. Alternatively, Michaiski and Olszyna [41] found dispersed M_6C particles in an as-deposited tungsten high speed steel (T1)-coating obtained by PPT. They explained this finding by heat accumulation in the coating induced by repeated plasma impulses. In the present work, the combination of "solute trapping" and cumulative heat-induced transformations was detected.

In the course of deposition of each layer, the previously deposited layer undergoes heating and deformation induced by plasma flux. This causes phase transformations in the heat-affected zone (HAZ), such as: (a) martensite tempering; (b) carbide precipitation from the austenite followed by (c) the transformation of the depleted austenite to ferrite. Owing to fast "heating-cooling", carbides precipitate as a fine cementite carbide network, as suggested by Fig.5c and the XRD pattern in Fig. 10a. (This carbide phase is kinetically more favorable because its formation does not require any substantial fluctuations of W and/or Cr atoms). Thus, a sandwich-like structure composed of alternating carbide-poor martensite/austenite (M/A) layers and HAZ layers forms (Fig. 13). The microhardness of carbide-poor (light contrast) bands is higher, which is attributed to the "austenite/martensite" structure. Darker HAZ–bands are somewhat softer (as aforementioned in 3.2), most likely because of partial martensite tempering and austenite→ferrite transformation. Hence, the above explanation accounts for the alternating grey-white bands observed in Fig. 5a.

4.2. Heat treated coating

The as-deposited coating is thermodynamically unstable due to the supersaturated solid solutions. It can turn to the stable state through carbide precipitation at temperatures of elevated Cr and/or W atoms diffusivity. In this work, stable state was attained by post-deposition heat treatment. Based on the calculated using Thermo-Calc the phase diagrams of Fig. 2, heating at 950 ^{o}C would lead to "austenite + M_7C_3" and "austenite + M_6C" for Cr28

and W18, respectively. The isothermal treatment in this area promoted the depletion of austenite by carbon and carbide-forming elements (W, Cr, Mn), leading to the formation of large number of carbides in the coating (compare Fig. 5a with Fig. 5c). The high temperature and prolonged isothermal treatment allowed the formation of thermodynamically stable carbides in accordance with the equilibrium phase diagrams (Fig. 2). Carbide precipitation led to a sharp increase in the coating microhardness: the microhardness of layers A and B (1250-1450 $HV_{0.05}$) is close to that of pure carbides M_7C_3 and M_6C (1600-1800 HV [42]). Thus, the post-deposition heat treatment is proved to be an important stage for coating property improving.

Isothermal HTs of as-cast HCCIs at 900-1000 ºC usually aim at the precipitation of fine secondary carbides of M_7C_3 and $M_{23}C_6$ stoichiometries [20, 22, 23, 43]. These have most likely nucleated as nanosized particles [44] mostly on defects inside austenite grains due to Cr atoms volume diffusion [23]. In contrast, in Cr28-deposited layers, precipitation has led to the formation of relatively coarse carbide particles in the form of a carbide network, as illustrated in Fig. 7a, b and Fig. 12a and c. Presumably, they nucleated at grain boundaries and their growth was controlled by a mechanism of grain boundary diffusion. Owing to a lower activation energy, this mechanism can provide the intensive diffusion flux of Cr atoms required for the formation of bulky carbides. Since austenite has variable carbon solubility, some dissolution of carbides could occur at 950 ºC. Regarding the HT W18-deposited layers, similar arguments can be raised bearing in mind that W18-steels in practice are subjected to hardening HT at 1200-1300 ºC, where carbides are dissolved in austenite, which, by quenching, is then transformed to a stable and hard martensite; tempering is applied at 550-600 ºC leading to precipitation of fine M_2C coexisting with remaining coarse primary M_6C carbides [45]. Based on: (a) the above facts, (b) the minimal content of W dissolved in the matrix of layer B (Table 3) and (c) the extensive presence of bulky M_6C in the microstructure of layer B, it is obvious that the microstructure of the HT W18-deposited layers is neither a case of carbide dissolution in matrix nor a case of tempering. Therefore, the kinetics of isothermal carbide precipitation

in the coating should further be studied. Such an approach will allow the selection of the optimal post-deposition heat treatment mode in order to obtain the maximum coating hardness.

The amount of carbides in the HT coating should also be discussed in further detail. As shown in Table 2, the carbide volume fractions in the coating layers are much higher (by 2-3 times) in comparison with those of W18 and Cr28 alloys (Table 1). This suggests that during PPT, a by-process has occurred leading to carbon enrichment of the coating in relation to the cathode materials. This process is most likely erosion of the inner channel walls of the EAPA by the pulsed plasma. Since the channel is made of paper-reinforced bakelite $(C_6H_6O{\cdot}CH_2O)_n$, carbon atoms can easily be released as a result of paper burning and polymer decomposition under high-current discharge. Released carbon atoms are transferred by the plasma flux to the substrate surface, where they saturate the liquid microdroplets of the cathode material. This extra-carbon causes the formation of extra carbide particles as compared to the carbide VF of the cathode materials which could improve the coating wear resistance (besides hardness). However, plasma-induced carbon enrichment may decrease ductility, a matter that may be faced with proper heat treatments. These issues are the subject of on-going research by the authors. It should be noted that even after ten depositions, the microstructure and the microhardness values were reproducible. Every ten depositions, the material of the tube walls was replaced in order to keep the microstructure and the related properties under close control.

It was also of interest to evaluate the carbon enrichment of the coating layers with respect to the cathode materials. For this purpose, Thermo-Calc calculations for Fe-28wt%Cr-2wt%Mn-1.3wt%Si-C alloys were carried out. The results of calculations are demonstrated in Fig. 14, in terms of mass fractions (MF) of carbide phases versus temperature in alloys with different carbon contents. As follows from Fig. 14, Thermo-Calc predicts the MF of $M_{23}C_6$ and M_7C_3 – at 2.2 wt% C (that corresponds to Cr28), and M_7C_3 – at 4.0 and 5.5 wt % C; total carbide mass fractions varied within the range of 35-67 wt%. In order to be able to compare the data with the carbide VFs in the coating layers (Table 3), MF was converted to VF

according to the following relation:

$$VF = \frac{\frac{MF_{M_7C_3}}{\rho_{M_7C_3}} + \frac{MF_{M_{23}C6}}{\rho_{M_{23}C_6}}}{\frac{MF_{M_7C_3}}{\rho_{M_7C_3}} + \frac{MF_{M_{23}C6}}{\rho_{M_{23}C_6}} + \frac{MF_{\gamma}}{\rho_{\gamma}}} \; 100\% \qquad (1)$$

where, MF_{γ}, $MF_{M_7C_3}$, $MF_{M_{23}C_6}$: mass fractions of austenite, carbides M_7C_3 and $M_{23}C_6$, accordingly; ρ_{γ}, $\rho_{M_7C_3}$, $\rho_{M_{23}C_6}$: density of austenite (7.85 g·cm^{-3}) and carbides ($\rho_{M_7C_3}$ = 6.97 g·cm^{-3}, $\rho_{M_{23}C_6}$ =7.20 g·cm^{-3} [38]). For the calculations of Fig. 14, it has been assumed that MF_{γ}, $MF_{M_7C_3}$ and $MF_{M_{23}C_6}$ are the values corresponding to the temperature of the eutectoid transformation initiation.

As seen in Fig. 14d, the calculated VF of the eutectic carbides in Cr28 (2.24 wt% C) is 35.8 vol. %, which is close to that of the VF value experimentally found in Cr28 (Table 1). According to the Thermo-Calc calculations (Fig. 14), the carbide VF values in Cr-based layers A and C (61.3 and 55.4 vol. %, respectively, Table 2) can be obtained when carbon contents are about 4.7 and 5.2 wt% respectively, which are quite higher than that of Cr28 material. Although the "austenite+M_7C_3" area at 950 ^{o}C covers a wide range of carbon content including 4.7-5.2 wt% (see phase diagram in Fig. 2b), these results are unexpected because they mean doubling of the carbon content during the PP treatment. The same doubts arise for W-based layers B and D since, according to the Fe-18%W-4%Cr-1%V-C phase diagram (Fig. 2a), M_6C at 950 ^{o}C appears only at carbon concentrations lower than 1.8 wt%C.

Considering the short time of the plasma jet action, the actual enrichment of coating with carbon should be much lower than the calculated values. It allows to assume that the carbide precipitation in the coating during HT resulted in the formation of larger amounts of

carbides depleted of carbide-forming elements. Indeed, Table 3 shows a significant Cr deficiency of M_7C_3 confirming the aforementioned assumption. The Cr content of M_7C_3 in layers A and C has been estimated as 30.2 and 31.5, respectively, which is much lower than that reported in previous works. More specifically, according to Laird II [46], the Cr-content of M_7C_3 in 3.2C-29Cr-HCCI is 60.9 wt%. Moreover, Filipovic et. al [47] found chromium concentration in M_7C_3 (2.9C-19Cr-HCCI) is in the range 39.8-53.36 wt%. Similar values (43.70-44.22 wt % Cr) have been reported for eutectic M_7C_3 in 2.7C-14.6Cr-HCCI [30]. Even if one considers that EDS measurements are erroneous due to matrix "effect", these values seem to be excessively low as compared with the just mentioned published values. (Here it should be noted that bulky carbide particle dimensions are higher or marginally within the limits of EDS spatial resolution; the EDS spatial resolution for high atomic number elements is reported as (0.2–1) μm^3 for high atomic number elements, for usual high voltage conditions (15–25 kV) [48]). Table 3 shows that the formation of M_7C_3 carbides in the coating involved much more iron atoms resulting in an iron content of 63.8-64.8 wt % (layers A and C). According to the carbide chemical composition in Table 3, the formula of M_7C_3 in the coating can be claimed as $(Fe_{4.8}Cr_{2.2})C_3$. Since iron largely replaced chromium in the carbides, more chromium was available to form new carbides increasing their VF in the coating. Similar arguments can be made for carbides M_6C in layers B and D: these carbides also seem depleted of tungsten, with respect to previous work [49]. In particular, the W content of M_6C in M2 tool steel, which has been reported as 37.81 wt % [49], is much higher than the one reported in the present effort. According to Table 7, M_6C formulas can be presented as $(Fe_{3.8}W_{1.4}Cr_{0.8})C$ for layer B and $(Fe_{4.4}WCr_{0.6})C$ for layer D. Thus, it can also be postulated that W was largely replaced by Fe in the M_6C lattice. Tungsten liberated to the matrix formed new carbide particles.

This work showed that pulse plasma technique using an electrothermal axial plasma accelerator can successfully be employed for the surface modification of and coating deposition on HCCIs. Using cathode with relatively low melting points allowed the formation

of a coating of about 100 μm thickness by relatively few plasma pulses. In the above context, the employment of eutectic phase containing alloys (high-Cr cast irons, high speed steels, multi-component cast alloys, etc.) as cathode materials seems promising in view of their relatively low solidus temperature and the ability to obtain wear resistant coatings with notably high amount of hard phases (carbides, borides, etc).

A comparison with results obtained earlier [50-52] using the EAPA device shows that the new approach for PPT proposed in the present work (low-melting cathode plus post-deposition HT) has some apparent advantages. For instance, Cheiliakh et al. [50] describe the coating obtained by EAPA using a titanium cathode without post-deposition HT. Due to a higher melting point (1668 ^{o}C), the titanium cathode led to the formation of a thinner coating (50-60 μm after 6 pulses), that is almost 1.5 times thinner than that of the present work. Secondly, the hardness of the Ti-based coating was 870-1000 HV, while in this study, the coating hardness has reached 1240-1445 HV.

The combination of cathode materials makes possible the production of a laminated coating structure with improved properties as compared to a single cathode material. Such coatings allow to conjoin the barrier layers of different functionalities depending on the application. In particular, in the conditions of impact loadings, the presence of a ductile layer under the wear-resistant brittle layer may inhibit the crack nucleation and prevent coating cracking. In the conditions of high-temperature application or severe sliding wear, the Cr-rich layer can protect coating from high-temperature oxidation and so on. The deposition of layers with different chemical compositions may induce mutual diffusion processes. A combination of functionalities is realized in this work by alternating Cr-rich and W-rich layers throughout the coating: layers A and C (Cr-rich) can act as corrosion protectors in oxidizing environments, while layer B (W-rich) has the highest microhardness owing to the presence of M_6C carbides with decreased iron content. Here it should be noted that although the substrate/coating interface is quite smooth, the following layer microstructure is more chaotic.

A question is arising, whether this microstructure can negatively affect the mechanical properties of the coating. The “substrate–coating” interface is formed under the first plasma impulse. The smoothness of its interface could be the outcome of substrate surface melting under plasma, followed by very fast solidification due to the low temperature of the substrate. This has led to the formation of a thin layer with a very fine crystalline structure where the substrate smoothly “transits” into the coating. At subsequent pulses, the previously deposited layers are in a higher temperature than the initial substrate temperature, which increases the rate of crystallization of deposited microdroplets. This promotes more pronounced mechanical mixing of droplets which leads to coarsening of microstructure. Despite this coarsening, the coating also includes fine dispersions of roundish precipitates (Fig. 7) that provide dispersion strengthening. Furthermore, the heat affected interlayers and transition layer E can provide strong metallurgical bonding. Also, the gradient composition smoothly adjusting to the composition of the substrate, provides strong evidence of the good coating/substrate adhesion, as noted in section 3.3, end of first paragraph and two last sentences. Finally, alloying of the metallic part of the carbides with W (Table 3) provides solid solution strengthening of the carbides. The above strengthening factors are surpassing the negative contribution of structure coarsening, as shown in Fig. 6b.

It should be emphasized that, not only is the heat treated coating much harder than its substrate but its hardness decreases with coating depth in a functionally gradient pattern; the latter allows for a more uniform stress distribution and good adhesion at the coating/substrate adhesion. Additional improvement of functional abilities of layered coating could be achieved by post-deposition HT which implies further intensive research.

Conclusions

1. An Fe-C-Cr-W coating of thickness 80-120 μm was deposited on 14.5wt%Cr-cast iron by pulsed plasma treatment employing an electrothermal axial plasma accelerator. The coating process was carried out by alternately depositing cathodes made of 18 wt%W-high speed steel

and 28 wt%Cr-cast iron.

2. PPT has led to modification of substrate sub-surface layer with formation of a zone that provided a smooth transition from the substrate to coating. Transition zones are noted between the upper coating layers as well, contributing to a smooth interlayer transition.

3. The as-deposited coating has a layered microstructure, consisting of intermittent "martensite/austenite" and heat-affected layers. The cross-sectional microhardness of the as-deposited coating varies in the range of 500-655 $HV_{0.05}$ to be being higher in the "martensite/austenite" layers.

4. Post-deposited HT has led to the precipitation of numerous carbide particles within the coating. In the layers deposited using W18 cathode, the carbides are of M_6C and M_2C types; in the layers deposited using Cr28 cathode, the carbides are of M_7C_3 (predominant amount) and $M_{23}C_6$ types. The layered alternation in the nature of the carbides resulted in a sharp increase in the coating microhardness up to 1240-1445 $HV_{0.05}$.

5. During PPT, plasma-due erosion of the inner channel walls of the EAPA under high-current discharge resulted in significant enrichment of the coating with carbon. This likely occurs due to discharge-induced erosion of the inner EAPA channel walls which promotes the release carbon atoms to be captured by the plasma flux. The carbon enrichment is responsible for the notable increase in the carbide volume fraction as compared to that of the cathode materials. As a result the carbides in coating are found to be Cr/W depleted in favor of Fe.

Acknowledgements

V.G. Efremenko, Yu.G. Chabak and V.I. Fedun would like to thank the Ministry of Education and Science of Ukraine for the financial support of project No. 0115U000172. They also thank Anatolii Rud' for editing text in English. The authors appreciate the help of Professor Hossam Halfa (Central Metallurgical Research and Development Institute, Cairo, Egypt) with thermodynamic calculations using Thermo-Calc software.

References

[1] Yong Xiang, Deping Yu, Qingtao Li, Huabei Peng, Xiuquan Cao, Jin Yao, Effects of thermal plasma jet heat flux characteristics on surface hardening, J. Mater. Process. Technol. 226 (2015) 238-246.

[2] S.S. Samotugin V.I. Lavrinenko, E.V. Kudinova, Yu. S. Samotugina, The influence of plasma surface modification process on the structure and phase composition of cutting-tool hardmetals, Journal of Superhard Materials. 33 (2011) P. 200-207.

[3] S. Semboshi, A. Iwase, T. Takasugi, Surface hardening of age-hardenable Cu–Ti alloy by plasma carburization, Surf. Coat. Technol. 283 (2015) 262-267.

[4] Y.Y. Özbek, H. Akbulut, M. Durman, Surface properties of M2 steel treated by pulse plasma technique, Vacuum. 122 Part A (2015) 90-95.

[5] N. Espallargas, S. Mischler, Dry wear and tribocorrosion mechanisms of pulse plasma nitrided Ni–Cr alloy, Wear. 270 (2011) 464-471.

[6] S. Romankov, A. Mamaeva, S.D. Kaloshkin, S.V. Komarov, Pulsed plasma treatment of Ti–Al coatings produced by mechanical alloying method, Mater. Lett. 61 (2007) 5288-5291.

[7] M. Kovaleva, Yu. Tyurin, N. Vasilik, O. Kolisnichenko, M. Prozorova, M. Arseenko, E. Danshina, Deposition and characterization of Al_2O_3 coatings by multi-chamber gas-dynamic accelerator, Surf. Coat. Technol. 232 (2013) 719–725.

[8] Yu.E. Kolyada, V.I. Fedun, Excitation of elastic pulses by powerful plasmoids in the acoustic waveguide, Probl. At. Sci. Technol., Ser.: Plasma Phys. 4 (2008) 260-263.

[9] Yu.E. Kolyada, V.I. Fedun, Pulse electrothermal plasma accelerators and its application in scientific researches, Probl. At. Sci. Technol., Ser.: Plasma Phys. 4 (2015) 325-330.

[10] Yu.E. Kolyada, V.I. Fedun, V.I. Tyutyunnikov, N.A. Savinkov, A.E. Kapustin, Formation mechanism of the metallic nanostructures using pulsed axial electrothermal plasma accelerator, Probl. At. Sci. Technol., Ser.: Plasma Phys. 4 (2013) 297-300.

[11] Y.E. Kolyada, A.A. Bizyukov, O.N. Bulanchuk, V.I. Fedun, Pulse electrothermal plasma accelerators and its application in the technologies, Probl. At. Sci. Technol., Ser.: Plasma Phys. 4 (2015) 319-324.

[12] S. N. Bratushka, Yu. N. Tyurin, O. V. Kolisnichenko, A. D. Mikhalev, R. Yu. Tkachenko, N. A. Makhmudov, A. V. Pshik, R. Denisenko, I. V. Yakushchenko Structure and tribological characteristics of steel under melting by plasma flow and simultaneous Mo and W alloying, Journal of Friction and Wear. 33 **(**2012) 22-33.

[13] Nana Zhao, Yunhua Xu, Lisheng Zhong, Yinglin Yan, Ke Song, Liuliu Shen, Vladimir E. Ovcharenko, Fabrication, microstructure and abrasive wear characteristics of an in situ tantalum carbide ceramic gradient composite, Ceram. Int. 41, Part A (2015) 12950-12957.

[14] C.A. León-Patiño, E.A. Aguilar-Reyes, E. Bedolla-Becerril, A. Bedolla-Jacuinde, S. Méndez-Díaz, Dry sliding wear of gradient Al-Ni/SiC composites, Wear. 301 (2013) 688-694.

[15] Fangxia Ye, Mirabbos Hojamberdiev, Yunhua Xu, Lisheng Zhong, Honghua Yan, Zhe Chen, $(Fe,Cr)_7C_3$/Fe surface gradient composite: Microstructure, microhardness, and wear resistance, Mater. Chem. Phys. 147 (2014) 823-830.

[16] Zhiwen Xie, Zhuangzhu Luo, Qin Yang, Tian Chen, Sheng Tan, Yunjiao Wang, Yimin Luo, Improving anti-wear and anti-corrosion properties of AM60 magnesium alloy by ion implantation and Al/AlN/CrAlN/CrN/MoS_2 gradient duplex coating, Vacuum. 101 (2014) 171-176.

[17] M. Fenech, B. Mallia, M. Grech, J.C. Betts, The post-deposition heat treatment of co-deposited Cr_3C_2 and AISI 410 stainless steel using the coaxial laser deposition technique, J. Mater. Sci. 48 (2013) 2224-2235.

[18] P. Cadenas, M. Rodriguez, M.H. Staia, Effect of post-deposition heat treatment on the sliding wear resistance of a nickel-based coating deposited using high velocity oxy-fuel. Welding International. 23 (2009) 763-772.

[19] V.G. Efremenko, K. Shimizu, A.P. Cheiliakh, T.V. Kozarevs'ka, Yu.G. Chabak, H. Hara, K. Kusumoto, Abrasive wear resistance of spheroidal vanadium carbide cast irons, Journal of Friction and Wear. 34 (2013) 466-474.

[20] A.E. Karantzalis, A. Lekatou, H. Mavros, High chromium white irons, microstructure, carbide precipitation, sub-critical heat treatment, austenite destabilization, Intern. J. Cast Research. 6 (2009) 448-456.

[21] V.G. Efremenko, K. Shimizu, A.P. Cheiliakh, T.V. Kozarevskaya, K. Kusumoto, K.Yamamoto, Effect of vanadium and chromium on the microstructural features of V-Cr-Mn-Ni spheroidal carbide cast irons, Int. J. Miner., Metall. Mater. 21 (2014) 1096-1108.

[22] A. E. Karantzalis, A. Lekatou, A. Kapoglou, H. Mavros, V. Dracopoulos, Phase transformations and microstructural observations during subcritical heat treatments of a high-chromium cast iron, J. Mater. Eng. Perform. 21 (2012) 1030-1039.

[23] V.G. Efremenko, Yu.G. Chabak, M.N. Brykov, Kinetic parameters of secondary carbide precipitation in high-Cr white iron alloyed by Mn-Ni-Mo-V complex, J. Mater. Eng. Perform. 22 (2013) 1378-1385.

[24] Xiu Cheng, Shubing Hu, Wulin Song, Xuesong Xiong, A comparative study on gray and nodular cast irons surface melted by plasma beam, Vacuum. 101 (2014) 177-183.

[25] Bong-Yong Jeong, Jeong-Ho Chang, Myung-Ho Kim, Thermal fatigue characteristics of plasma duplex treated nodular cast irons, Surf. Coat. Technol. 205 (2010) 896-901.

[26] V. Efremenko, K. Shimizu, Yu. Chabak, Effect of destabilizing heat treatment on solid-state phase transformation in high-chromium cast irons, Metall. Mater. Trans. A. 44 (2013) 5434-5446.

[27] H. Halfa, Thermodynamic calculation for silicon modified AISI M2 high speed tool steel, J. Miner. Mater. Charact. Eng. 1 (2013) 257-270.

[28] H. Halfa, Three main solidification reactions of vanadium modified T1–tungsten high speed tool steel, in: Metal 2015, Brno, Czech Republic, 2015.

[29] G. F. Vander Voort, Metallography, Principles and Practice, ASTM International, 1999.

[30] V. G. Efremenko, Yu. G. Chabak, A. Lekatou, A. E. Karantzalis, A. V. Efremenko, High-temperature oxidation and decarburization of 14.55 wt pct Cr-cast iron in dry air atmosphere, Metall. Mater. Trans. A. 47A (2016) 1529-1543.

[31] Yu.G. Chabak, Solid-state phase transformation in metallic matrix of high-chrome cast iron in subcritical temperature range, Metallofiz. Noveishie Tekhnol. 37 (2015) 1349-1367.

[32] G.A. Roberts, R. Kennedy, G. Krauss, Tool Steels, fifth ed., ASTM International, 1998.

[33] G.E. Totten, L.C. Casteletti, F.A.P. Fernandes, J. Gallego, Microstructural characterization of layers produced by plasma nitriding on austenitic and superaustenitic stainless steel grades, J. ASTM Int. 9 (2011) 1-11.

[34] Lihe Qian, Xiaoyong Feng, Fucheng Zhang, Deformed microstructure and hardness of Hadfield high manganese steel, Mater. Trans. 52 (2011) 1623-1628.

[35] A. Lekatou, R.D. Walker, Mechanism of solid state reduction of chromite, Ironmaking-Steelmaking, 22 (1995) 393-404.

[36] S.R. Shatynski, The Thermochemistry of Transition Metal Carbides, Oxidation of Metals, 13 (1979) 105-118.

[37] P. Rolland, V.L. Carlino, R. Vane, Improved Carbon Analysis with Evactron Plasma Cleaning, Microsc. Microanal., 10 (Suppl. 02) (2004) 964-965.

[38 H.O. Pierson, Handbook of Refractory Carbides & Nitrides: Properties, Characteristics, Processing and Applications, Noyes Publications, 1996.

[39] I. Hemmati, V. Ocelık, J. Th. M. De Hosson, Microstructural characterization of AISI 431 martensitic stainless steel laser-deposited coatings, J. Mater. Sci. 46 (2011) 3405-3414.

[40] B. Vamsi Krishna, A. Bandyopadhyay, Surface modification of AISI 410 stainless steel using laser engineered net shaping (LENS^{TM}). Mater. Des. 30(2009) 1490–1496.

[41] A. Michaiski, A. Olszyna, Layers of high speed steel with microstructures characteristic of heat-treated materials, Surf. Coat. Technol. 59 (1993) 287-289.

[42] M.F. Buchely, J.C. Gutierrez, L.M. Leon, A. Toro, The effect of microstructure on abrasive wear of hardfacing alloys, Wear. 259 (2005) 52–61.

[43] A.E. Karantzalis, A. Lekatou, E. Diavati, Effect of destabilization heat treatments on the microstructure of high-chromium casti: A microscopy examination approach, J. Mater. Eng. Perform. 8 (2009) 1078–1085.

[44] Y.G. Chabak, V.G. Efremenko, Change of secondary-carbides' nanostate in 14.5% Cr cast iron at high-temperature heating, Metallofiz. Noveishie Tekhnol. 34 (2012) 1205-1220.

[45] T. V. Rajan, C. P. Sharma, Ashok Sharma, Heat Treatment: Principles and Techniques, 2nd ed., PHI Learning Pvt. Ltd., New Delhi, pp.241-242.

[46] G. Laird II, Microstructures of Ni-hard I, Ni-hard IV and high-Cr white cast irons, Transactions of AFS, 99 (1991) 339-357.

[47] M. Filipovic, E. Romhanji, Z. Kamberovic, Chemical composition and morphology of M_7C_3 eutectic carbide in high chromium white cast iron alloyed with vanadium, ISIJ Int. 52 (2012) 2200–2204.

[48] G. Wille, X. Bourrat, N. Maubec, R. Guegan, A. Lahfid, Raman-in-SEM studies of inorganic materials, in: J. Yarwood, R. Douthwaite, S.B. Duckett (Eds.), Spectroscopic Properties of Inorganic and Organometallic Compounds: Techniques, Materials and Applications, The Royal Society of Chemistry, London, 2014, pp. 79–116.

[49] A. S. Chaus, Microstructural and properties evaluation of M2 high speed steel after inoculating addition of powder W and WC, Mater. Sci. Technol. 30 (2014) 1105-1115.

[50] A. P. Cheiliakh, Yu. Yu. Kutsomelya, V. I. Fedun, M. A. Ryabikina, The structure and properties of steel 40Kh after pulsed plasma processing using titanium electrodes, Science and Education a New Dimension Natural and Technical Science. 8 (2013) 79-84.

[51] N. O. Savinkov, Yu. E. Kolyada, The allocation of the micro-hardness of steel under pulsed plasma treatment, Reporter of the Priazovskyi State Technical University 29 (2014) 70-80.

[52] A. P. Cheiliakh, Yu. Yu Kutsomelya., V. I. Fedun, M. A. Ryabikina, The influence of parameters of pulse-plasma treatment on structure and properties of steel 40Cr, Building, Materials Science, Mechanical Engineering 73 (2014) 235-239.

Table 1

Chemical compositions (wt%) and CVFs (vol. %) of substrate and cathode materials

	Materials	C	Cr	W	Mn	V	Si	Ti	Ni	CVF
Substrate	HCCL	2.60	14.50	-	3.96	0.10	1.38	0.10	0.21	-
Cathode	W18	0.75	3.85	17.92	0.34	1.07	0.30	-	-	16.0
Cathode	Cr28	2.34	27.39	-	3.13	-	1.26	0.20	-	34.5

Table 2

The average precipitate volume fractions (vol.%) in the HT coating layers.

Layers	A	B	C	D	E
CVF	61.3±3.0 / 15.2±1.1*	51.7±4.0	55.4±3.2	43.9±4.3	21.7±3.5

* as-deposited state

Table 3

Chemical composition of matrix and carbide phases in the HT coating (wt.%).

Layer	Phase	Cr	W	Si	Mn	Fe	Carbide formulae
A	Matrix	25.6±1.0	-	1.6±0.1	1.5±0.3	71.3±2.1	-
	Bulky carbides	30.2±2.5	3.0±0.8	1.0±0.1	2.0±0.2	63.8±1.2	$(Fe_{4.8}Cr_{2.2})C_3$
B	Matrix	13.9±2.5	0.9±0.3	1.6±0.2	0.5±0.1	83.1±3.5	-
	Bulky carbides	26.9±0.4	15.4±0.5	-	2.4±0.1	55.3±0.8	$(Fe_{3.8}W_{1.4}Cr_{0.8})C$
	Fine carbides	12.4±0.9	40.3±1.6	-	0.2±0.1	47.1±3.1	-
C	Matrix	22.3±1.5	-	1.7±0.2	1.3±0.2	74.6±2.8	-
	Bulky carbides	31.5±1.9	1.2±0.1	-	2.5±0.4	64.8±0.9	$(Fe_{4.8}Cr_{2.2})C_3$
D	Matrix	4.4±0.4	11.9±1.9	2.0±0.3	0.4±0.1	81.3±3.2	-
	Bulky carbides	10.5±0.2	16.9±0.5	-	0.5±0.1	72.1±0.7	$(Fe_{4.4}WCr_{0.6})C$
	Fine carbides	1.9±0.3	28.4±1.7	-	0.4±0.1	69.2±2.6	-

LIST OF FIGURES CAPTIONS

Fig. 1. (a) EAPA principle scheme: 1- paper reinforced bakelite tube, 2 – cathode, 3 and 4 - steel shells, 5 - exit edge, 6 - sheet copper cylinder; (b) the diagram of the EAPA electrical installation.

Fig. 2. Phase diagrams: (a) Fe-18%W-4%Cr-1%V-C, (b) Fe-28%Cr-2%Mn-1.3%Si-C.

Fig. 3. The initial microstructure of (a) substrate (HCCI), (b) cathode W18, and (c) cathode Cr28 (P, A: pearlite, austenite accordingly).

Fig. 4. XRD-pattern of Cr28 material; γ-Fe (4-0829), $(Cr,Fe)_7C_3$ (5-0720), Cr_3C_2 (5-0677).

Fig. 5. The microstructure of coating and substrate (optical, cross-section): (a, b, c) as-deposited, (d) heat-treated (4 vol. % Nital). (c) presents the microstructure within the circle shown in (b).

Fig. 6. The microhardness profile of coating and substrate (in cross-section): (a) as-deposited, (b) heat-treated.

Fig. 7. The microstructure of coating (SEM, cross section, HT state): (a) layer A, (b) layer B, (c) layer C, (d) layer D, (e) layer E.

Fig. 8. (a) SEI-image of the coating cross-section (after HT) and (b) corresponding EDX mapping of Cr, W and Fe.

Fig. 9. D/E interlayer area: (a) SEI-image, (b) BSE-image illustrating layer D (lighter contrast) and layer E (darker contrast).

Fig. 10. XRD-patterns of (a) as-deposited layer A, (b) HT layer A and (c) HT layer D; α-Fe (6-0696), γ-Fe (4-0829), $(Cr,Fe)_7C_3$ (5-0720), Cr_3C_2 (5-0677), Fe_3C (35-0772), $Cr_{23}C_6$ (35-0783), Fe_3W_3C (3-0980), W_2C (2-1134).

Fig. 11. Indicative points of EDS analysis in coating layers (a) A, (b) B, (c) C and (d) D.

Fig. 12. EDS spectra showing qualitative chemical composition of distinct constituents in layer D: (a) matrix, (b) bulky carbide, (c) fine carbide.

Fig. 13. The as-deposited coating structure.

Fig. 14. (a-c) Phase mass fractions for Fe-28%Cr-C system: (a) 2.2 wt %C, (b) 4 wt% C, (c) 5.5 wt% C. (d) CVF as a function of the carbon content.

FIGURES

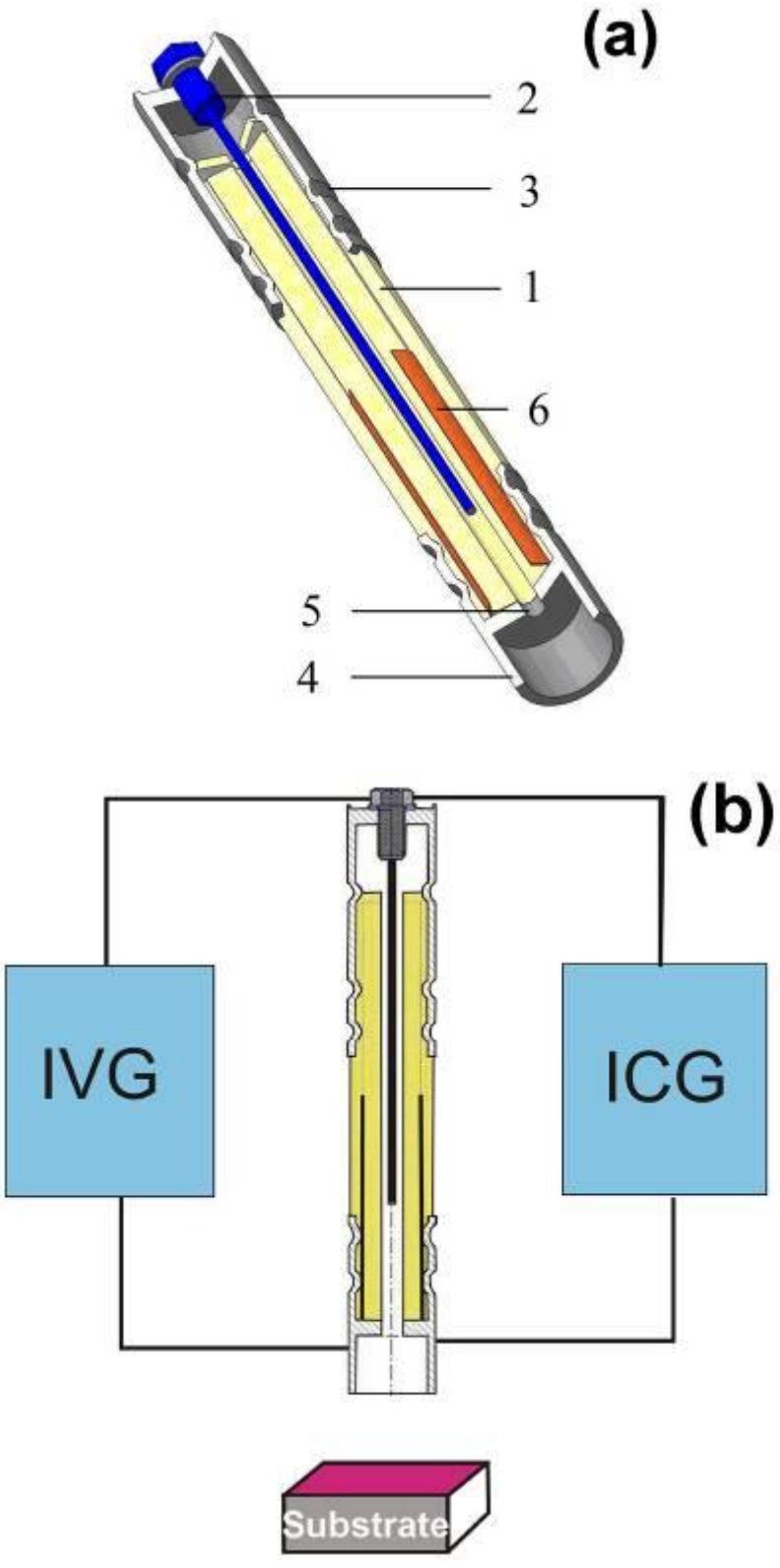

Fig. 1

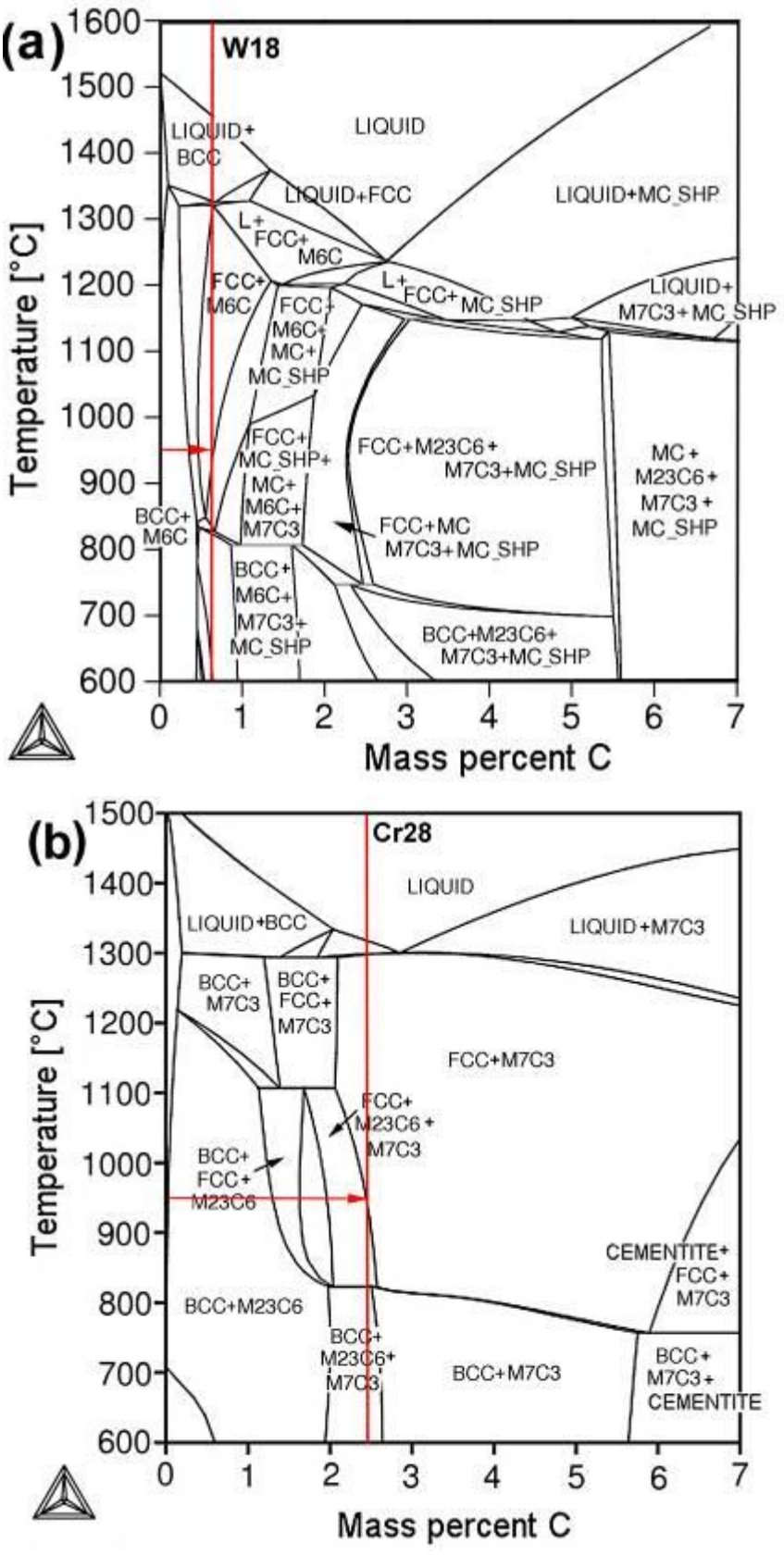
(a)
W18
LIQUID
LIQUID+ BCC
LIQUID+FCC
LIQUID+MC_SHP
L+ FCC+ M6C
L+ FCC+ MC_SHP
LIQUID+ M7C3+MC_SHP
FCC+ M6C
FCC+ M6C+ MC+ MC_SHP
FCC+ MC_SHP+ MC+ M6C+ M7C3
FCC+M23C6+ M7C3+MC_SHP
MC+ M23C6+ M7C3+ MC_SHP
BCC+ M6C
FCC+MC M7C3+MC_SHP
BCC+ M6C+ M7C3+ MC_SHP
BCC+M23C6+ M7C3+MC_SHP
Temperature [°C]
Mass percent C
(b)
Cr28
LIQUID
LIQUID+BCC
LIQUID+M7C3
BCC+ M7C3
BCC+ FCC+ M7C3
FCC+M7C3
FCC+ M23C6+ M7C3
BCC+ FCC+ M23C6
CEMENTITE+ FCC+ M7C3
BCC+M23C6
BCC+ M23C6+ M7C3
BCC+M7C3
BCC+ M7C3+ CEMENTITE
Temperature [°C]
Mass percent C

Fig. 2

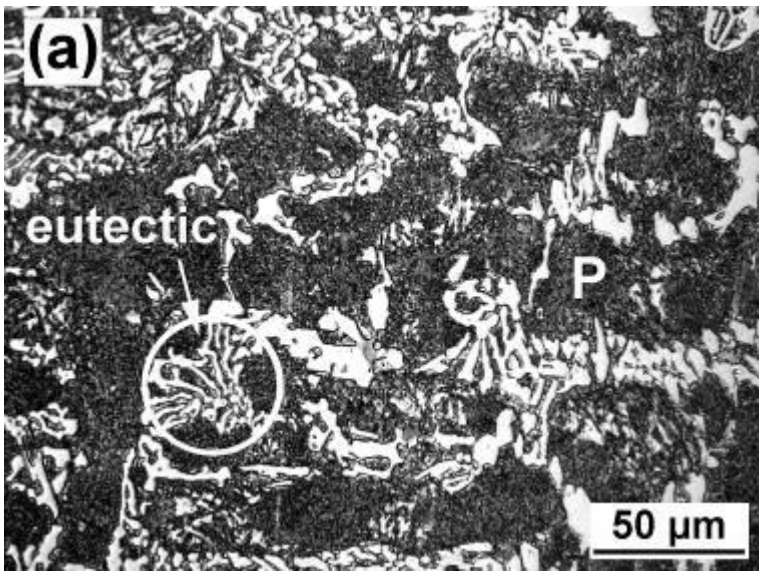

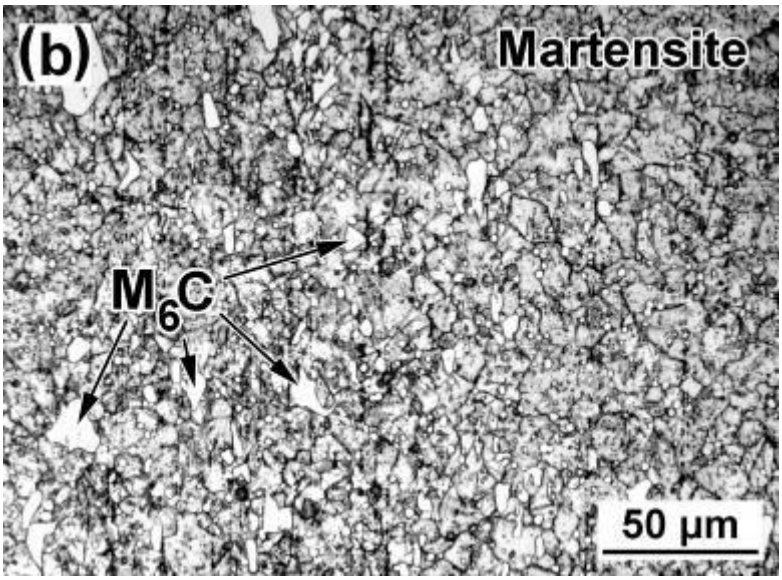

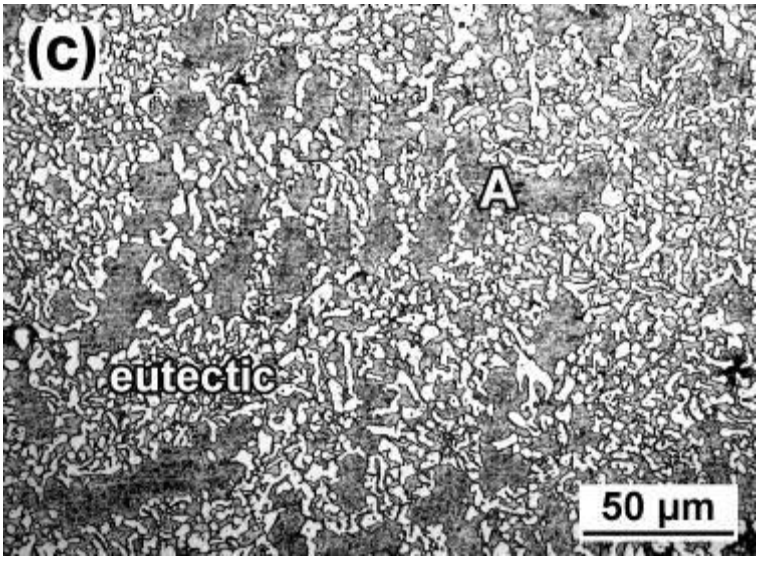

Fig.3

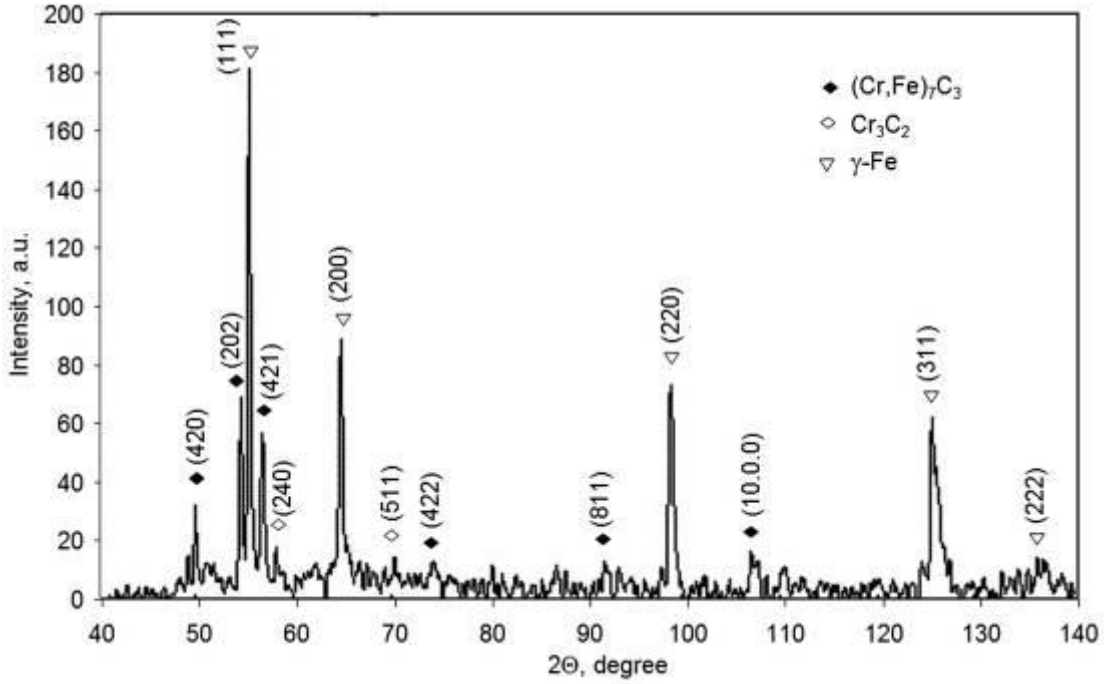
Intensity, a.u.
2Θ, degree
(Cr,Fe)7C3
Cr3C2
γ-Fe
(111)
(202)
(420)
(421)
(240)
(200)
(511)
(422)
(811)
(220)
(10.0.0)
(311)
(222)

Fig. 4.

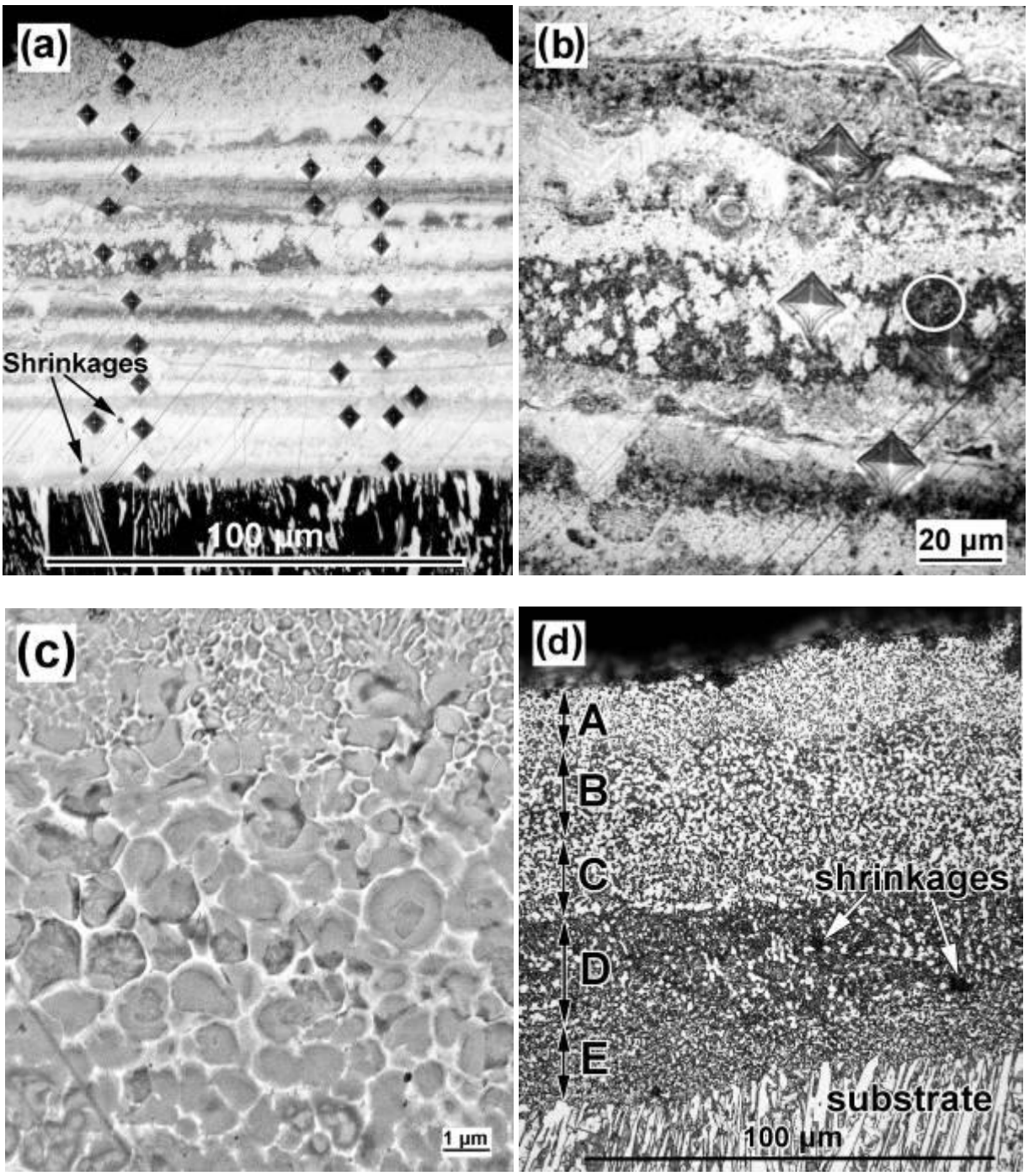
(a)
Shrinkages
100 µm
(b)
20 µm
(c)
1 µm
(d)
A
B
C
D
E
shrinkages
substrate
100 µm

Fig. 5.

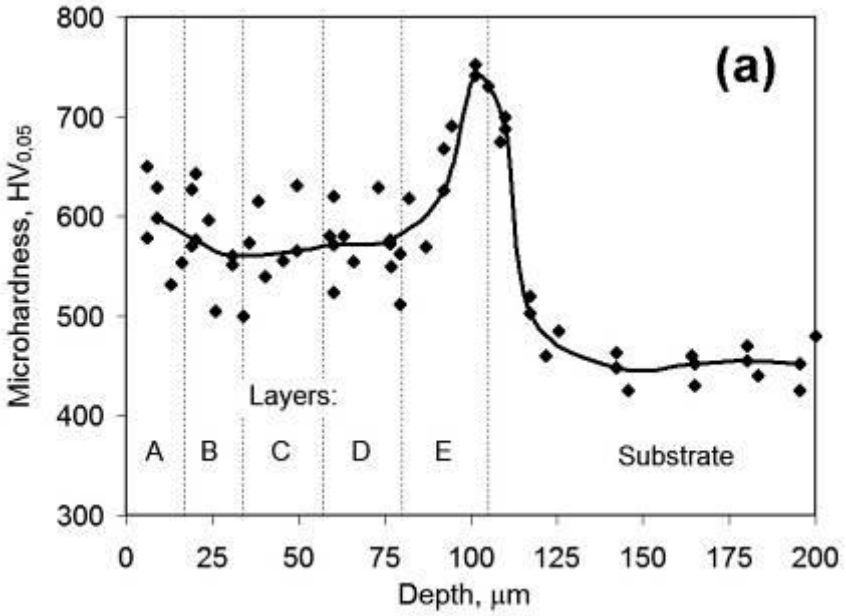
(a)
Microhardness, HV0,05
800
700
600
500
400
300
Layers:
A
B
C
D
E
Substrate
0
25
50
75
100
125
150
175
200
Depth, μm

1

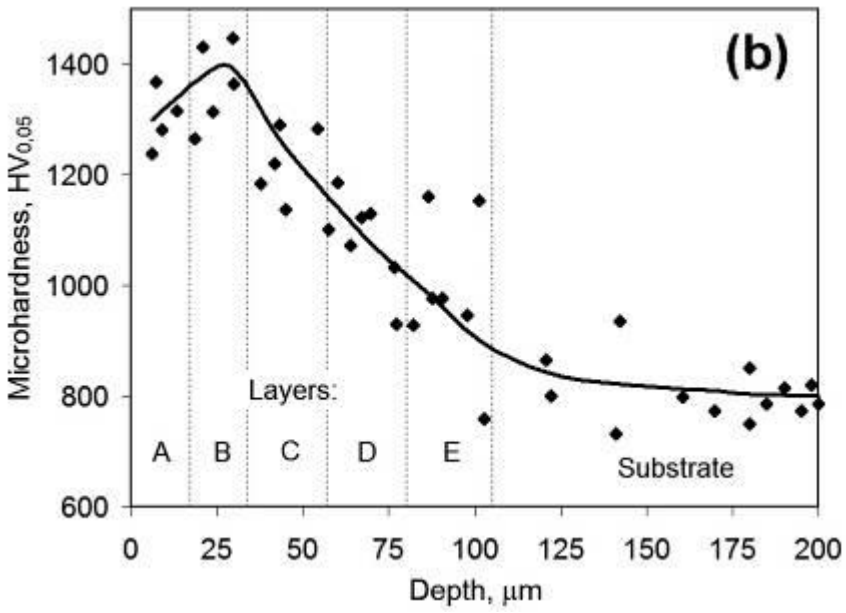
(b)
Microhardness, HV0,05
1400
1200
1000
800
600
Layers:
A
B
C
D
E
Substrate
0
25
50
75
100
125
150
175
200
Depth, μm

2

3 **Fig.6.**

4

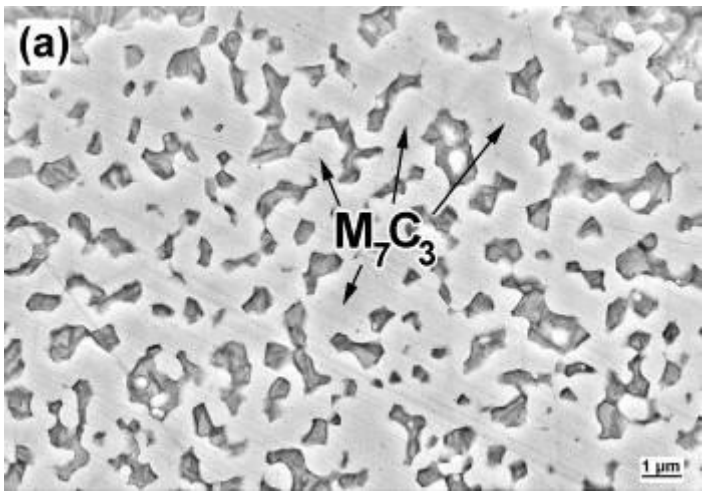

1

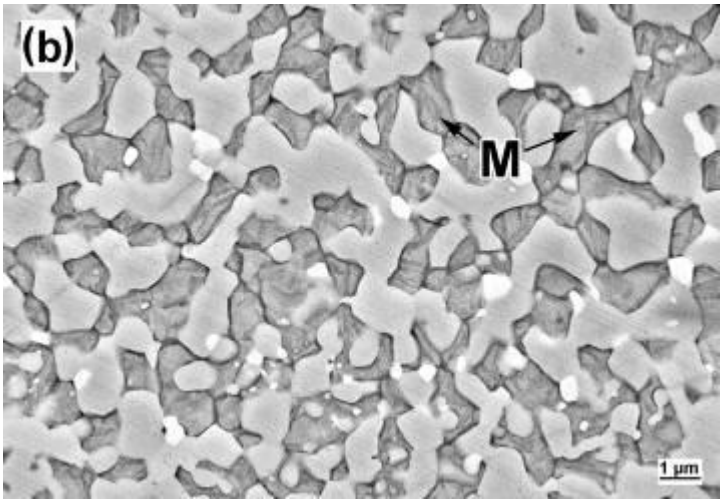

2

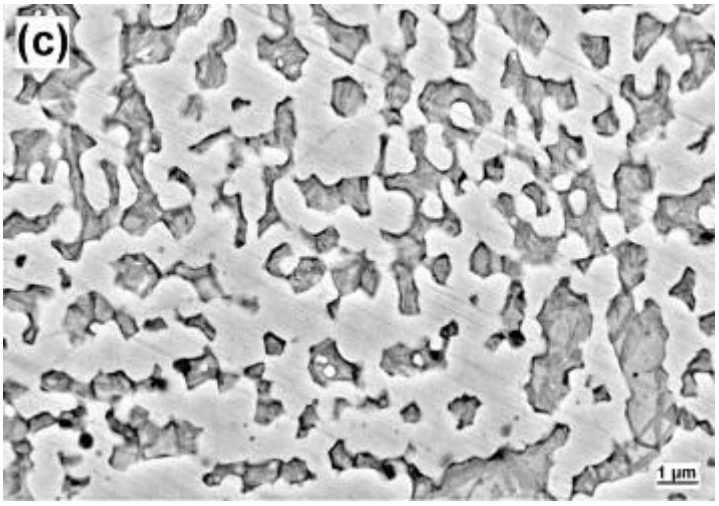

3

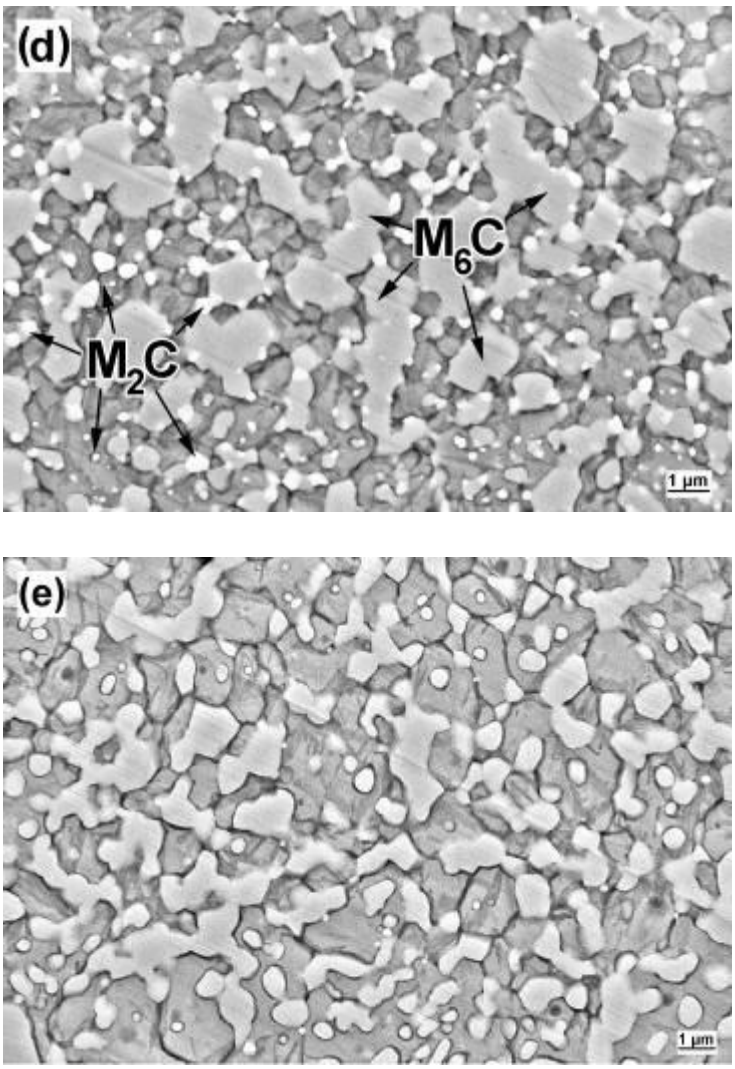

Fig. 7.

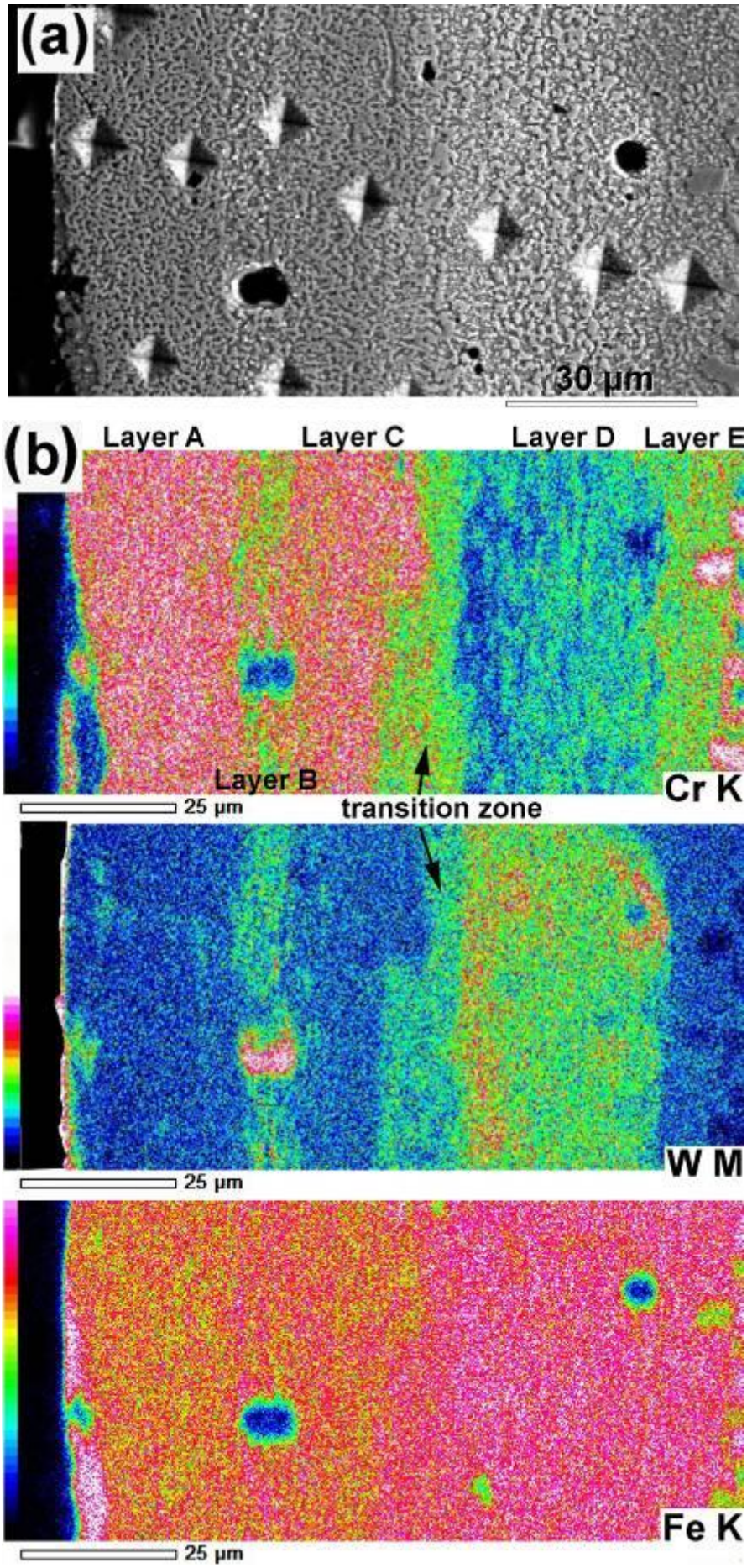
(a)
30 μm
(b)
Layer A
Layer C
Layer D
Layer E
Layer B
transition zone
Cr K
25 μm
W M
25 μm
Fe K
25 μm

Fig. 8.

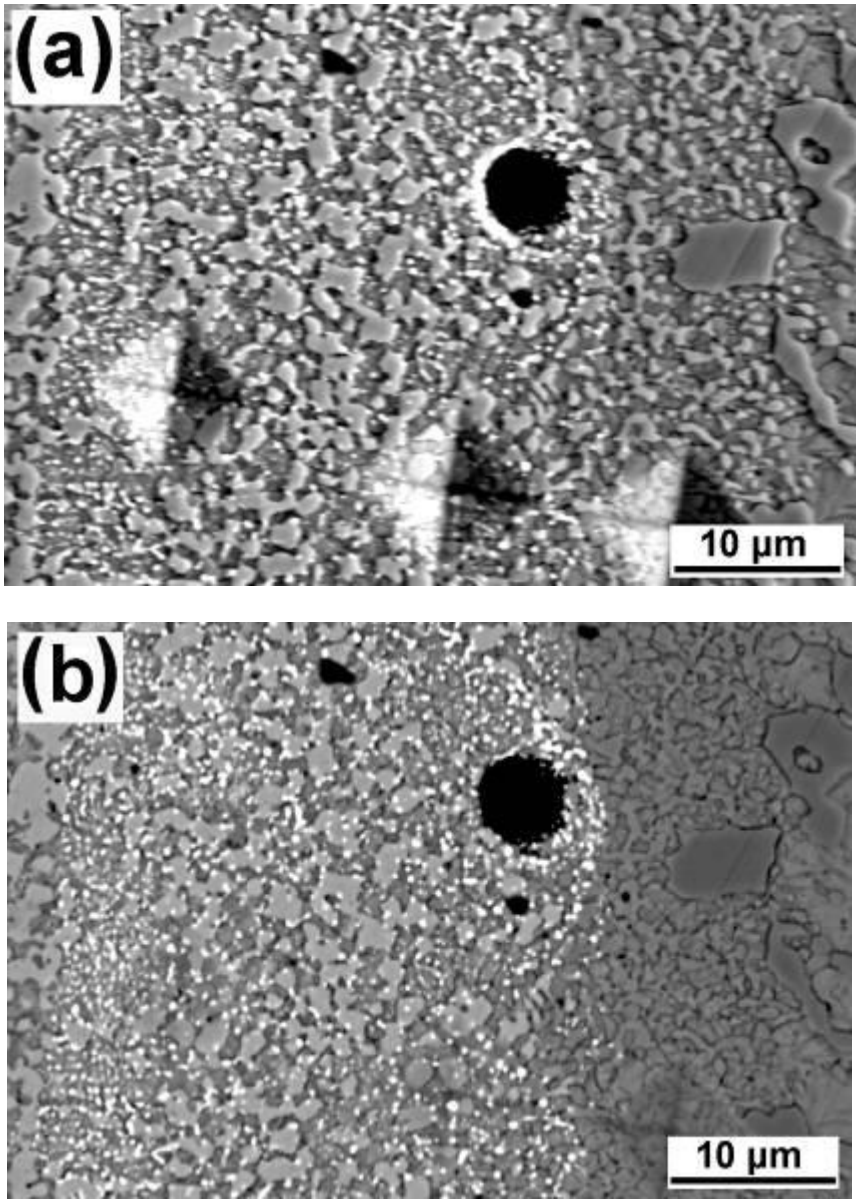

Fig. 9.

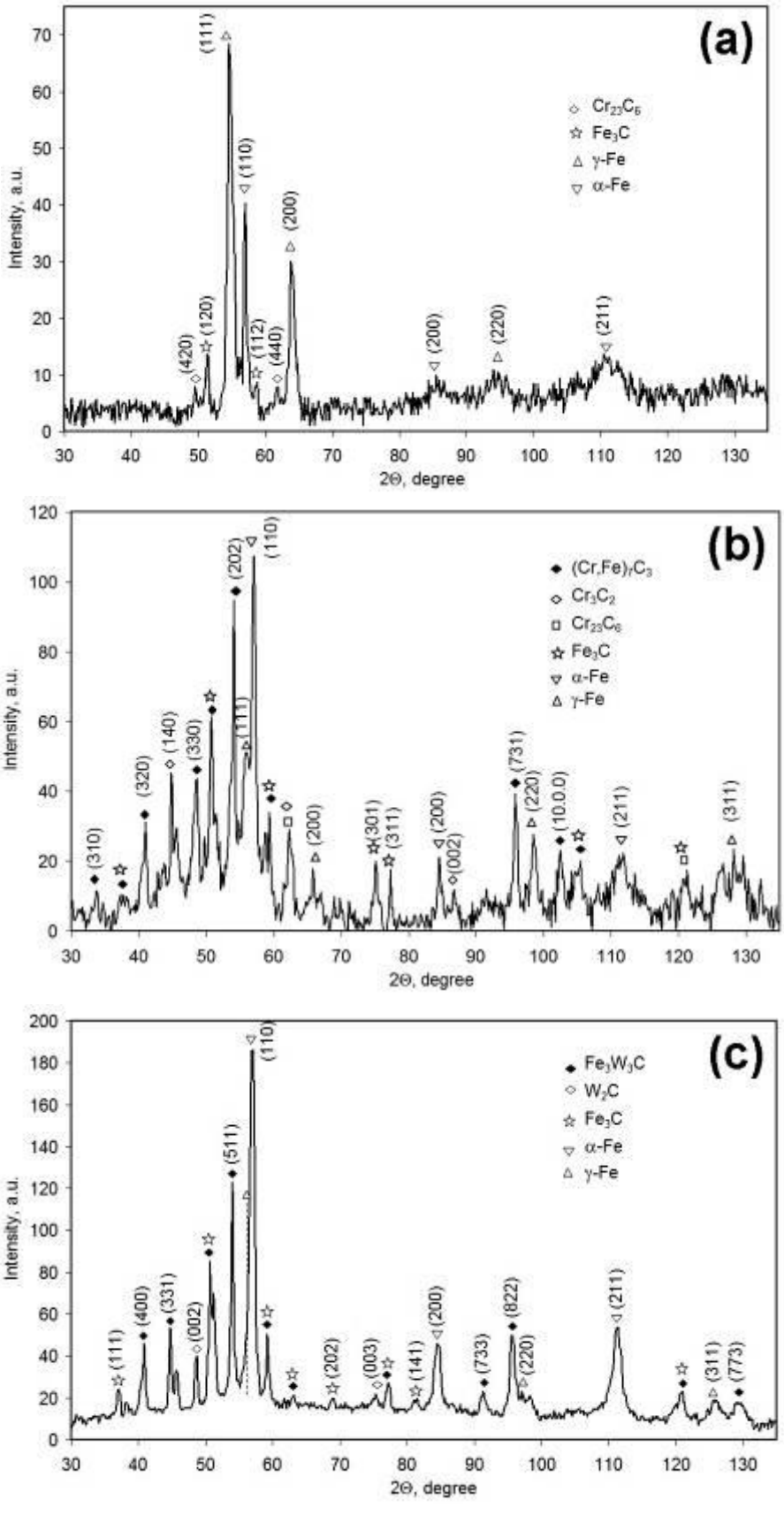
(a)
Cr23C6
Fe3C
γ-Fe
α-Fe
(111)
(110)
(200)
(420)
(120)
(112)
(440)
(200)
(220)
(211)
Intensity, a.u.
2Θ, degree
(b)
(Cr,Fe)7C3
Cr3C2
Cr23C6
Fe3C
α-Fe
γ-Fe
(202)
(110)
(320)
(140)
(330)
(111)
(310)
(200)
(301)
(311)
(200)
(002)
(731)
(220)
(10.0.0)
(211)
(311)
Intensity, a.u.
2Θ, degree
(c)
Fe3W3C
W2C
Fe3C
α-Fe
γ-Fe
(110)
(511)
(111)
(400)
(331)
(002)
(202)
(003)
(141)
(200)
(733)
(822)
(220)
(211)
(311)
(773)
Intensity, a.u.
2Θ, degree

Fig. 10.

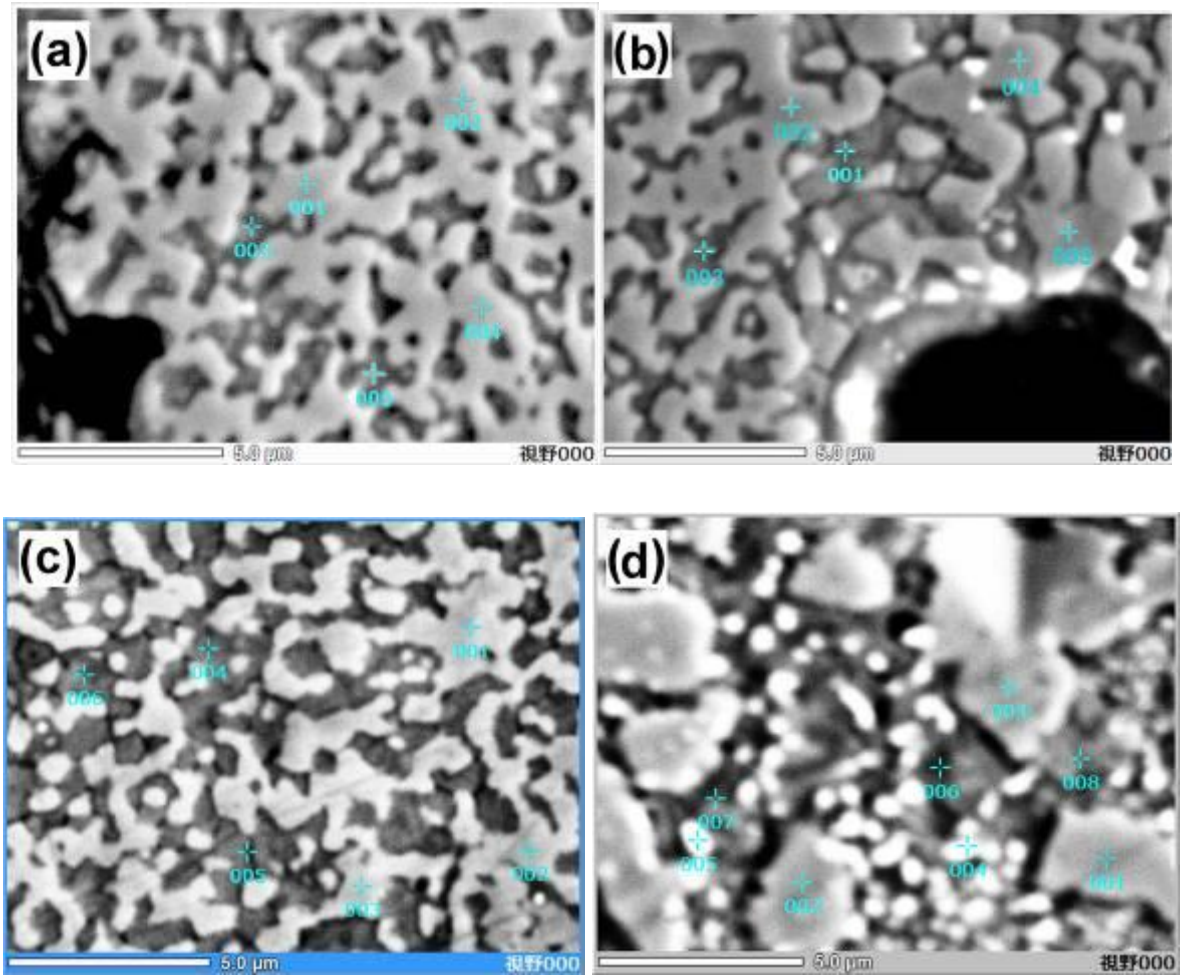

Fig. 11.

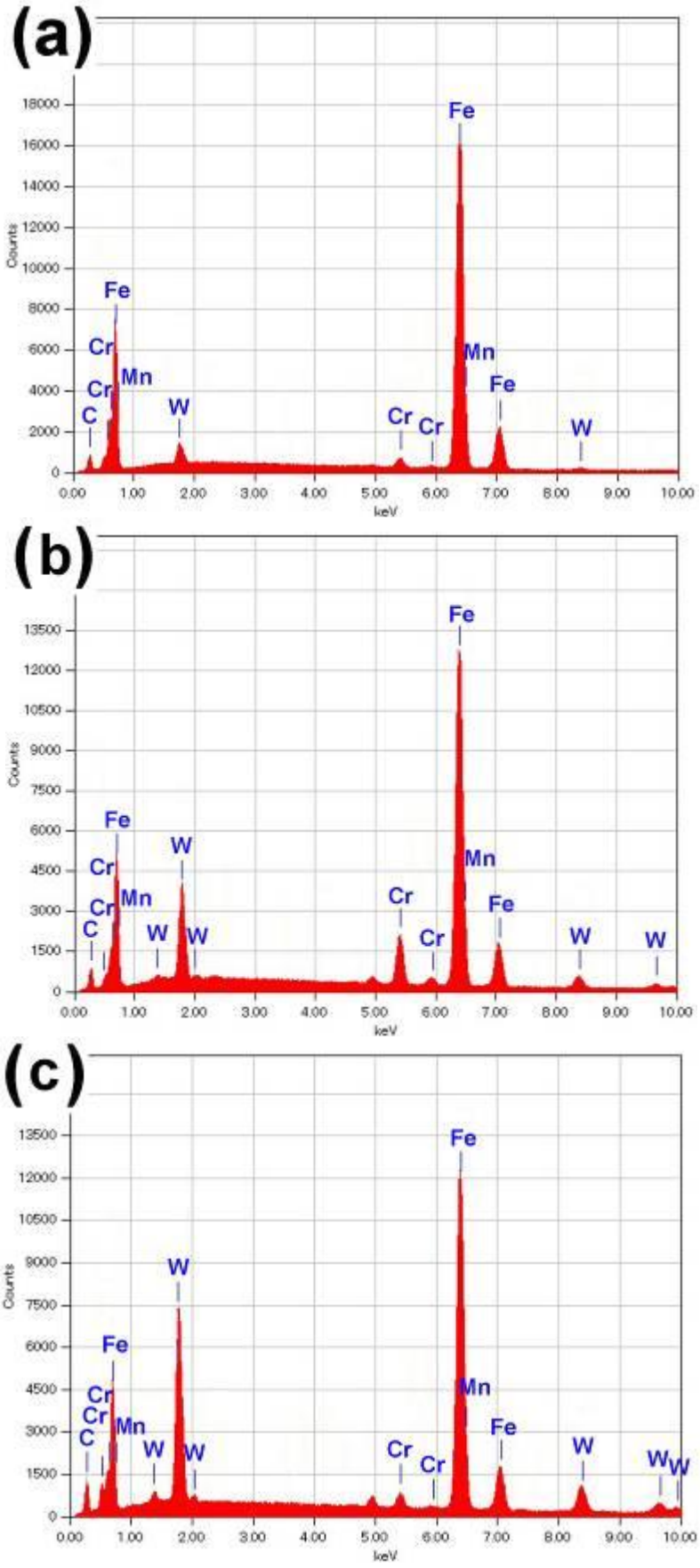
(a)
Counts
keV
Fe
Cr
Mn
W
C
(b)
Counts
keV
Fe
Cr
Mn
W
C
(c)
Counts
keV
Fe
Cr
Mn
W
C

Fig.12.

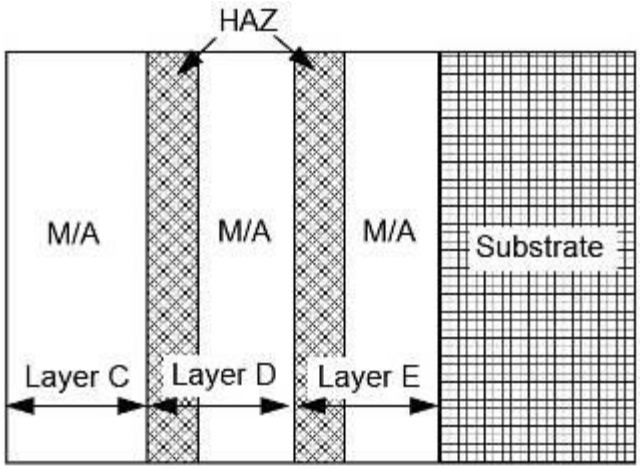
HAZ
M/A
M/A
M/A
Substrate
Layer C
Layer D
Layer E

Fig.13.

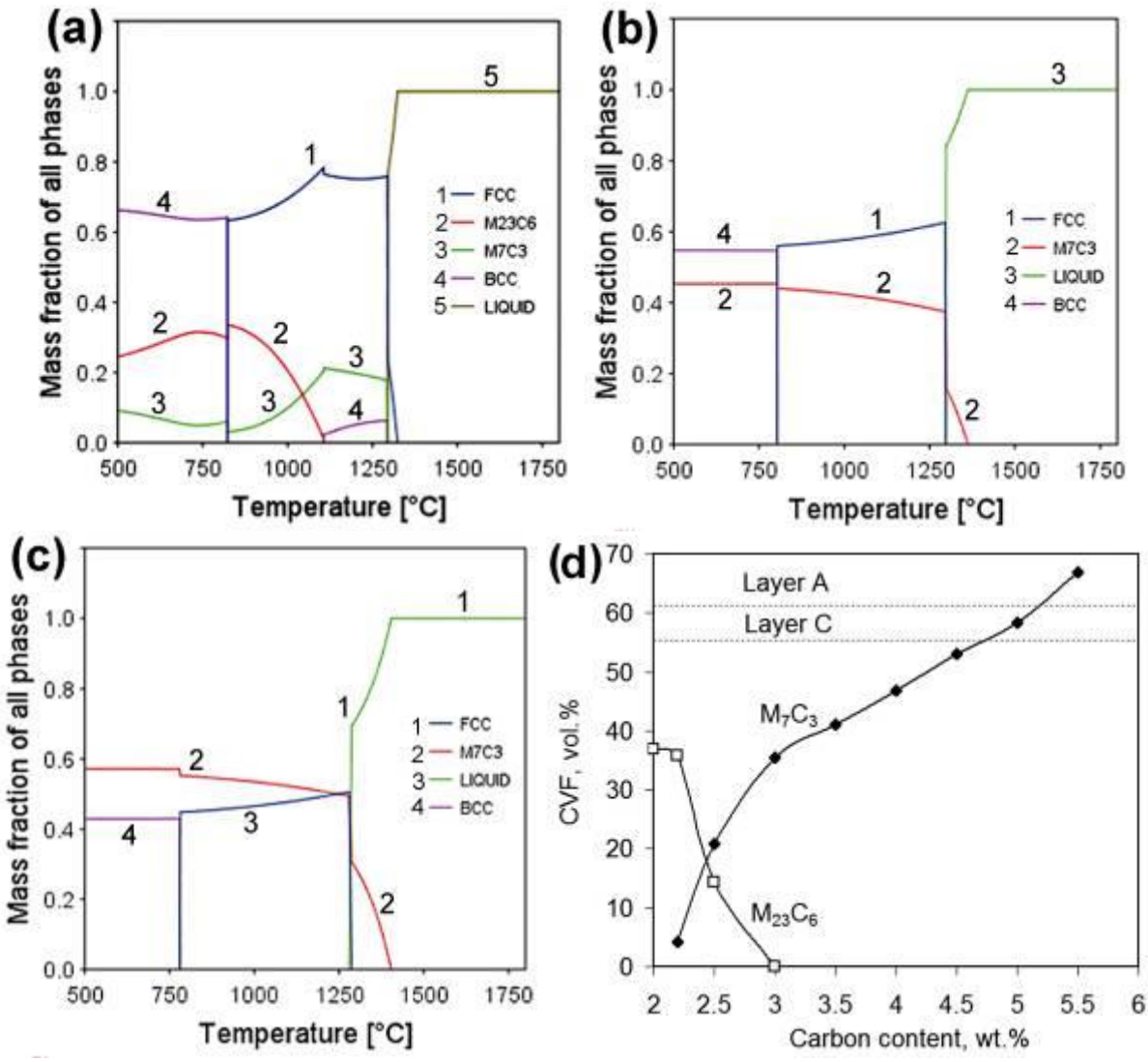
(a)
Mass fraction of all phases
Temperature [°C]
1 FCC
2 M23C6
3 M7C3
4 BCC
5 LIQUID
(b)
Mass fraction of all phases
Temperature [°C]
1 FCC
2 M7C3
3 LIQUID
4 BCC
(c)
Mass fraction of all phases
Temperature [°C]
1 FCC
2 M7C3
3 LIQUID
4 BCC
(d)
Layer A
Layer C
M7C3
M23C6
CVF, vol.%
Carbon content, wt.%

Fig. 14.

Highlights

- A Fe-C-Cr-W coating was deposited on high-Cr cast iron by pulsed plasma treatment.
- Alternating cathode material led to a layered coating structure.
- A plasma modified layer provided a smooth substrate-to-coating transition.
- Post-deposition heat treatment led to a layered carbide precipitation in the coating.
- The carbide content in the coating was much higher than that of the cathode material.